Mineralogy and Petrology (2018) 112 (Suppl 1):S149–S167
https://doi.org/10.1007/s00710-018-0613-8

ORIGINAL PAPER

The involvement of diamond-forming fluids in the metasomatic 'cocktail' of kimberlite sources

Yaakov Weiss [1,2] · Steven L. Goldstein [1,3]

Received: 14 December 2017 / Accepted: 20 June 2018 / Published online: 2 July 2018

Abstract

Microinclusion-bearing diamonds offer the opportunity to investigate relationships between mantle metasomatism, diamond formation and kimberlite eruptions in intracratonic provinces. We have analyzed a suite of 7 microinclusion-bearing diamonds from the Finsch Group II kimberlite, South Africa, and identified two diamond populations: 'Finsch IaA' diamonds have nitrogen solely in A-centers and contain saline high-density-fluid (HDF) microinclusions, while 'Finsch IaAB' diamonds have nitrogen in both A- and B-centers (25–35% B-centers) and are characterized by carbonatite HDF compositions. Based on nitrogen aggregation states and estimates for mantle residence temperatures, we conclude that 'Finsch IaA' diamonds formed during a young saline metasomatic event that preceded kimberlite eruption by ~50 kyr to 15 Myr. The possible timing of metasomatism and formation of 'Finsch IaAB' diamonds by carbonatite HDFs is less constrained, and could have taken place between ~15 Myr and 2 Gyr before eruption. Two of the diamonds encapsulated omphacite microinclusions in association with saline or low-Mg carbonatitic-like HDF. We observe compositional differences for Al_2O_3 vs. CaO between these metasomatised omphacites, and also compared to omphacites in mantle eclogites which were identified as metasomatised by kimberlite or high-Mg carbonatite; suggesting a possible relationship between Al_2O_3 and CaO in metasomatised omphacite and the type of fluid/melt it interacted with. The combined data for microinclusion-bearing diamonds from the Finsch Group II kimberlite and the neighbouring Group I kimberlites at Koffiefontein and De Beers Pool indicate that a substantial volume of the southwest Kaapvaal deep lithosphere was impacted by saline metasomatism during Cretaceous time, and a direct relationship between saline metasomatism, diamond formation and the Kaapvaal late-Mesozoic 'kimberlite bloom'. We therefore conclude that saline HDFs play a key role in the buildup of metasomatic mantle sources leading to kimberlite eruptions.

Keywords Metasomatism · Diamond-forming fluids · Kimberlite · Finsch · Clinopyroxene · Kaapvaal · Lithosphere

Introduction

Carbon- and water-rich (C-O-H) fluids in Earths' mantle play major roles in Earth processes (e.g. mantle melting) and the transport of volatiles and trace elements between different mantle and crustal reservoirs, as well as the atmosphere, as part of the global circulation of volatiles. C-O-H fluids are commonly involved in mantle metasomatism and diamond formation (e.g. Dawson 1984; Deines 1980; Green and Wallace 1988; Luth 1993; Menzies and Wass 1983; Schneider and Eggler 1986; Stachel et al. 2004; Wass et al. 1980; Wyllie 1977), and are often encapsulated as fluid microinclusions in a fast-growing form of diamonds – 'fibrous diamonds' (Navon et al. 1988). Many fibrous diamonds capture both mineral microinclusions, which represent the

Editorial handling: T. Stachel

Electronic supplementary material The online version of this article (https://doi.org/10.1007/s00710-018-0613-8) contains supplementary material, which is available to authorized users.

✉ Yaakov Weiss
yweiss@ldeo.columbia.edu

[1] Lamont-Doherty Earth Observatory of Columbia University, 61 Route 9W, P.O. Box 1000, Palisades, NY 10964, USA

[2] The Freddy and Nadine Herrmann Institute of Earth Sciences, The Hebrew University, The Edmond J. Safra Campus - Givat Ram, 91904 Jerusalem, Israel

[3] Department of Earth and Environmental Sciences, Columbia University, 61 Route 9W, P.O. Box 1000, Palisades, NY 10964, USA

diamond mantle host rock, and HDF microinclusions, which are remnants of the metasomatic agent (e.g. Izraeli et al. 2004; Tomlinson et al. 2009; Weiss et al. 2015). These diamonds thus capture a 'snapshot' of metasomatic fluid-rock interaction (Tomlinson et al. 2009), and their study permits a glimpse of past episodes of mantle metasomatism, whereby circulating deep C-O-H HDFs interact with mantle rocks and form diamonds.

Diamond-forming HDFs vary between four compositional end-members: saline HDFs that carry mostly K, Na, Cl and water with some carbonates and silicates; high-Mg carbonatitic HDFs characterized by high MgO and carbonate, and low silica, alumina and water; and a continuous array between silicic and low-Mg carbonatitic HDF end-members, with varying amounts of silicates, carbonates and water (e.g. Klein-BenDavid et al. 2009; Navon et al. 1988; Skuzovatov et al. 2016; Smith et al. 2012; Tomlinson et al. 2006; Weiss et al. 2009). All four HDF-types are generally highly enriched in most incompatible elements compared to 'primitive mantle' (PM) values and are characterized by two main trace-element patterns: one with high field strength element (HFSE) depletions and high large ion lithophile element (LILE) enrichments, similar to calcalkaline magmas and continental rocks; the other with smaller enrichments in LILE elements and smaller depletions in HFSE, and thus 'smoother' overall trace-element patterns similar to oceanic basalts (e.g. Tomlinson et al. 2009; Weiss et al. 2013). Variations between the two patterns have been explained in several ways, for example: Tomlinson et al. (2009) suggested wall-rock reaction and fractional crystallization of carbonatite fluids to explain variations in LILE and light rare earth elements (LREEs); Klein-BenDavid et al. (2007), Zedgenizov et al. (2009) and Rege et al. (2010) preferred fractional crystallization and immiscibility between end-member compositions, or mixing between different HDFs, while Weiss et al. (2009, 2013) suggested percolation and interaction of HDFs with mantle rocks as the reason for observed trace element compositional changes. Incompatible element enrichment in mantle minerals reflects such HDF-rock interaction (e.g. Menzies and Wass 1983; Smit et al. 2014; Viljoen et al. 2014; Stachel et al. 2004; Tomlinson et al. 2009), and the impact of this process in shaping metasomatic mantle reservoirs.

Petrologic and geochemical evidence connects kimberlites and mantle metasomatism (Greenwood et al. 1999; Kamenetsky et al. 2004; van Achterbergh et al. 2004), and experimental studies, emphasize the necessity of enriched mantle in the formation of kimberlitic melts (Brey et al. 2008; Dalton and Presnall 1998; Le Roex et al. 2003). The occurrence of diamond ages older than their host kimberlite eruption age (e.g. Gurney et al. 2010; Kramers 1979; Richardson et al. 1984), has resulted in a consensus that diamonds are xenocrysts in kimberlites. However, the broad similarity of REE patterns between silicic to low-Mg carbonatitic HDFs and kimberlite magmas has been argued to represent a genetic relation between diamond-forming fluids and kimberlites at depth (Akagi and Masuda 1988; Schrauder et al. 1996). When the comparison is made for high-Mg carbonatite compositions, the resemblance in trace element patterns between HDFs and kimberlites is even more striking, and differences appear mainly in the overall enrichment factors and fractionation levels between highly incompatible and more compatible elements (Weiss et al. 2011). This observation was used by Weiss et al. (2011) to argue that high-Mg carbonatitic HDFs and kimberlites can be best understood as reflecting different melting regimes affecting the same (or very similar) metasomatised source compositions.

Here we report major- and trace-element data for HDFs and mineral microinclusions in seven microinclusion-bearing fibrous diamonds from the Finsch Group II kimberlite, South Africa. We document two diamond populations differing in their nitrogen aggregation state and HDF compositions, and discuss the type and timing of the metasomatic events in which they grew. Combining our data and results on microinclusion-bearing diamonds from neighboring kimberlites (Koffiefontein and De Beers Pool), we explore the recent sequence of metasomatism in the sub-continental lithospheric mantle (SCLM) of the southwest Kaapvaal Craton, and the relationship between HDF metasomatism, diamond formation, and kimberlite eruptions in this lithospheric province.

Samples and analytical techniques

Samples

Seven microinclusion-bearing diamonds from the Finsch Group II kimberlite, South Africa, were analyzed for the present study. The diamonds vary in weight between 12 and 76 mg, and have grey-white to dark grey color. Four diamonds are 'cloudy' (ON-FCH-350, 354, 355 and 356), they have dodecahedral morphology and contain an internal microinclusions-bearing part; two diamonds (ON-FCH-351, 352) show a cube-like habit and one is a hailstone boart with irregular morphology (ON-FCH-349). Each diamond was laser-cut twice to create a thin plate that was polished on both sides (Fig. 1). They were then cleaned ultrasonically in a mixture of HF 60% and HNO_3 69% for 2 h and washed with ethanol and distilled water before analysis. Fourier-transform infrared (FTIR) spectroscopy, electron probe microanalysis (EPMA) and laser ablation inductively coupled plasma mass spectrometry (LA-ICP-MS) analyses were performed to collect data on the nitrogen concentrations and aggregation states in the different diamonds, and the major and trace element compositions and volatile contents of the microinclusions they carry.

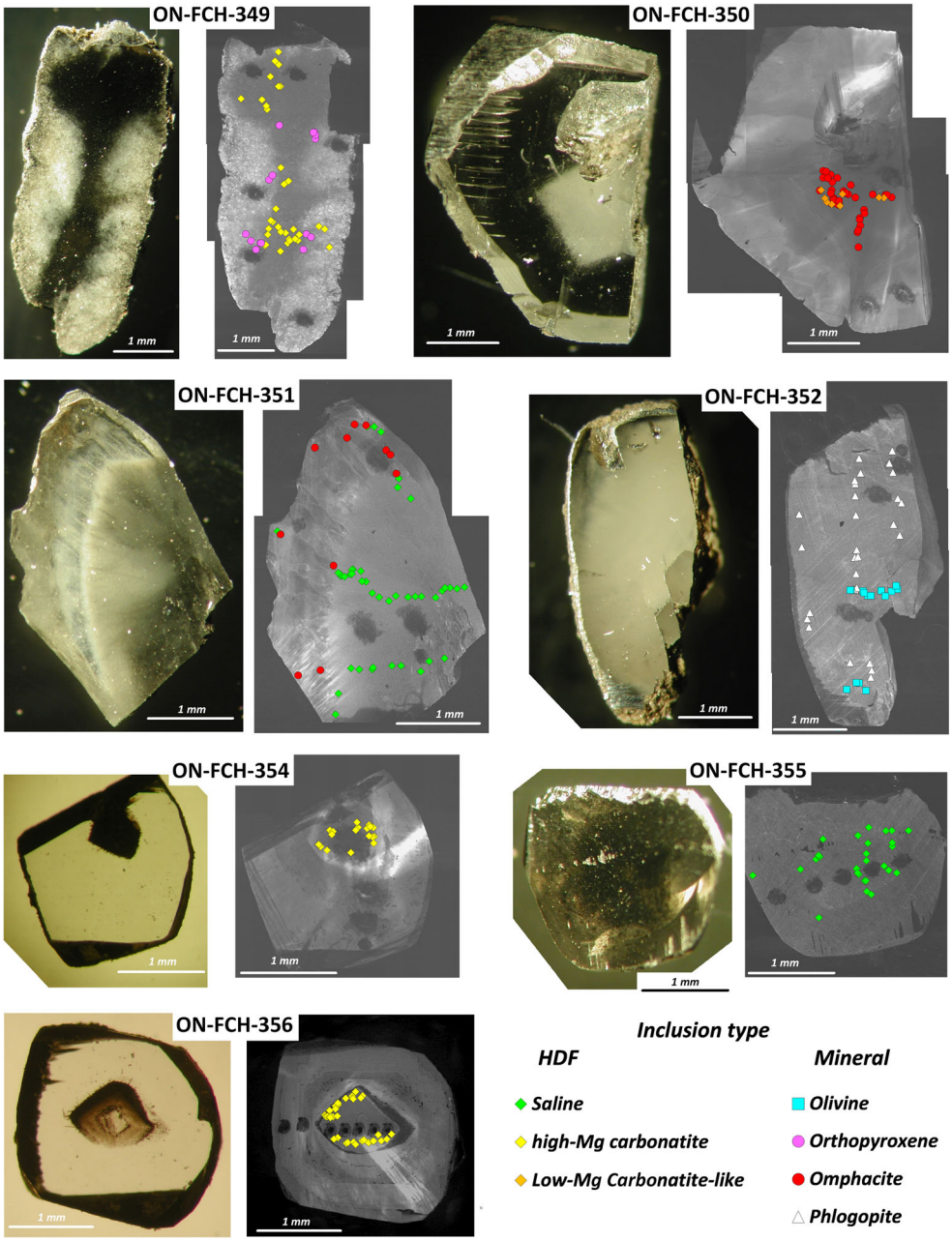

Fig. 1 Photomicrograph and cathodoluminescence (CL) images of microinclusion-bearing diamonds from the Finsch Group II kimberlites. The location and type (i.e. mineral or HDF) of the microinclusions that were analyzed by EPMA in each diamond are superimposed on its CL image. Pits on CL images were excavated during laser ablation ICP-MS analysis

Fourier-transform infrared (FTIR) spectroscopy

Infrared spectra were collected using a Bruker IRscope II microscope coupled to a Nicolet 740 FTIR spectrometer (Globar source, KBr beamsplitter, MCT detector, He–Ne laser). Spectra were taken in the range of 550–4000 cm^{-1} with a resolution of 2 cm^{-1}. Nitrogen concentrations and aggregation states (Table 1) were determined with a modified version of the DiaMap freeware (Howell et al. 2012; Daniel Howell and Yaakov Weiss, unpublished data), using the absorption coefficients of A-centers (double substitution of carbon atoms by two nitrogen atoms, Type IaA spectrum), B-centers (clusters of 4 nitrogen atoms and an atomic vacancy substituting 5 carbon atoms, Type IaB spectrum) and C-centers (single nitrogen replacing a carbon atom, Type Ib spectrum) (Boyd et al. 1994; Kiflawi et al. 1994; Boyd et al. 1995). Prior to deconvolution, the DiaMap program subtracts the intrinsic diamond absorption spectrum (Type IIa spectrum) and corrects the baseline for the raw data automatically (using a spline fit to the lowest points). The DiaMap spectral fitting range for nitrogen was set manually, to minimize the effects on the deconvolution process from partial overlapping absorbances of silicates, carbonates and apatite from the microinclusions. Absorbance due to C-centers was not detected in the Finsch diamonds. Uncertainties on the A- and B-centers concentrations were determined to be <5%. This was achieved by

Table 1 Nitrogen content and aggregation state of Finsch diamonds, and average composition of HDF microinclusions

Diamond	ON-FCH-349	ON-FCH-350	ON-FCH-351	ON-FCH-352	ON-FCH-354	ON-FCH-355	ON-FCH-356
Morphology	Amorphous (granular)	Dodecahedral (cloudy)	Cubic (broken)	Cubic (broken)	Dodecahedral (cloudy)	Dodecahedral (cloudy)	Dodecahedral (cloudy)
No. of IR spectra collected	2	2	2	3	3	1	2
Total N (ppm)	490 (1)[a]	1410 (31)	113 (0)	378 (1)	545 (33)	177	612 (11)
%N as B	26 (0)[b]	33 (1)	0 (0)	0 (0)	35 (1)	0	27 (4)
Platelet	+++	+++	–	–	+++	–	+++
Fluid type	High-Mg carbonatite	Low-Mg carbonatite-like	Saline	No HDF microinclusions	High-Mg carbonatite	Saline	High-Mg carbonatite
No. of inclusions analyzed	34	8	42	–	20	28	33
Composition (EPMA results; wt%) [c]							
SiO_2	7.6 (2.3)	11.4 (9.9)	4.9 (2.9)		5.1 (2.4)	5.2 (3.5)	5.3 (2.6)
TiO_2	1.0 (1.5)	2.1 (2.0)	0.7 (1.2)		1.2 (1.8)	1.2 (2.2)	2.2 (1.1)
Al_2O_3	1.0 (1.0)	1.6 (1.9)	1.1 (1.5)		1.4 (1.0)	1.4 (1.6)	1.2 (0.7)
FeO	6.7 (2.4)	16.2 (6.1)	13.7 (5.3)		5.8 (3.1)	9.2 (5.0)	7.6 (2.2)
MgO	24.1 (2.0)	2.2 (2.1)	1.3 (2.3)		18.3 (3.6)	2.1 (1.9)	21.9 (4.2)
CaO	20.2 (3.4)	23.2 (5.6)	3.2 (2.0)		12.5 (3.4)	6.0 (2.7)	14.1 (3.1)
BaO	4.4 (2.7)	–	0.9 (1.7)		14.3 (7.8)	1.9 (2.6)	11.6 (4.1)
Na_2O	3.5 (1.8)	5.6 (3.6)	11.6 (8.8)		1.3 (1.3)	8.0 (3.5)	1.4 (0.6)
K_2O	26.0 (2.8)	8.7 (3.7)	34.0 (8.5)		29.8 (7.0)	43.1 (6.7)	25.8 (4.4)
P_2O_5	2.4 (1.8)	2.3 (2.7)	0.9 (1.8)		0.9 (0.9)	1.9 (2.1)	1.9 (1.0)
Cl	4.0 (1.5)	34.4 (7.8)	35.9 (5.8)		12.2 (4.1)	25.7 (5.8)	9.2 (3.7)
Total[d]	4.1 (2.2)	2.0 (0.9)	3.8 (2.3)		4.0 (1.9)	3.9 (3.7)	5.2 (2.8)
CMF[e]	0.49 {0.54}	–	0.10 {0.13}	–	0.43 {0.49}	0.13 {0.16}	0.51 {0.57}
CO_2[f]	30.2 {30.9}	–	6.3 {6.7}	–	25.0 {25.7}	10.3 {10.9}	28.2 {28.9}
H_2O[g]	12.9 {10.8}	–	23.2 {18.3}	–	13.6 {11.0}	28.1 {23.5}	11.1 {8.9}
Mineral microinclusions[h]	Opx	Cpx	Cpx	Ol + Phl	–	–	–

[a] Average of total nitrogen (in ppm) and its standard deviation

[b] Average % of nitrogen that is present as B-centers and its standard deviation

[c] Normalized to 100 wt% on a water and carbonate free basis, with excess oxygen for chlorine. Standard deviations are quoted in brackets

[d] Initial analytical totals of oxides and Cl (wt%) before normalization

[e] CMF=$CO_2/(CO_2 + H_2O)$ molar ratio, as calculated from the IR spectrum, using $\varepsilon_{calcite}1433\ cm^{-1} = 739$ and $\varepsilon_{water}3420\ cm^{-1} = 87$ (AU·l/mol·cm) or $\{\varepsilon_{water}3420\ cm^{-1} = 109\}$ (Weiss et al. 2010; Venyaminov and Prendergast 1997; Thompson 1965). The CMF of ON-FCH-350 of the 'Finsch IaAB' diamonds could not be determined due to the low absorbance of carbonate and water in its IR spectrum

[f] CO_2 (wt%) in HDF, calculated according to the molar proportion of $CO_3 = Mg + Fe + Ca + Ba + Na/2 + K/2 + 2Ti\text{-}Cl/2\text{-}5P/3\text{-}(5Si + 9Al)/8\text{-}(Si + Al)/8$ for high-Mg carbonatite (Klein-BenDavid et al. 2009), and $CO_3 = Mg + Fe + Ca + Ba + (Na + K - Cl\text{-}Si/3)/2 - 5P/3\text{-}(Si\text{-}2 \times Ti\text{-}(Al\text{-}Si/3) \times 3/2)$ for saline HDF composition (Weiss et al. 2018)

[g] H_2O (wt%) in HDF, calculated from the molar CO_2 value and the $CO_2/(CO_2 + H_2O)$ ratio

[h] Orthopyroxene (OPX), clinopyroxene (CPX), olivine (Ol), phlogopite (Phl)

increasing and decreasing the amount of IaA and IaB that are subtracted until a clear peak or a 'negative' peak was observed at 1282 cm^{-1} (A-centers) and 1332 cm^{-1} (B-centers).

After baseline correction and subtraction of both diamond and nitrogen bands, the concentrations of water and carbonate were determined using the maximum absorbance of water and carbonate and their absorption coefficients (Weiss et al. 2010). These concentrations were used to calculate the carbonate mole fraction (CMF) of the trapped fluids [CMF = carbonate/(water+carbonate) molar ratio; Table 1]. Absorption peaks, known to be caused by primary mineral microinclusions trapped by the diamond during its growth, as well as daughter mineral phases that grew from the trapped HDFs within the microinclusions, were documented and used to confirm the general characteristics of the host rock mineralogy and the nature of the diamond-forming fluids.

Cathodoluminescence (CL) imaging and electron probe microanalysis (EPMA)

Cathodoluminescence imaging (total intensity at 400–700 nm) of the diamonds was recorded using a Gatan MiniCL attached to a JEOL JXA 8600 EPMA. The acceleration voltage was 25 kV and the beam current was 75 nA. These images provide the internal structure of the diamond and allow the determination of the exact location of the microinclusions relative to the growth history of the diamond (Fig. 1).

The major element compositions of the microinclusions were determined using a JEOL JXA 8600 EPMA equipped with a Pioneer-Norvar EDS (133 eV) detector. Backscattered electron imaging was used to detect shallow, subsurface microinclusions (<2 μm depth). Each inclusion was analyzed for 100 s using an acceleration voltage of 15 kV and a beam current of 10 nA. The electron beam size was 1 μm. A set of reference materials were used for calibration. Olivine was used to calibrate Si-Kα, corundum for Al-Kα, hematite for Fe-Kα, calcite for Ca-Kα, apatite for P-Kα, sodalite for Cl-Kα, spinel for Mg-Kα, rutile for Ti-Kα, chromite for Cr-Kα, benitoite for Ba-Lα, sodalite for Na-Kα and orthoclase for K-Kα. The spectral data were reduced using the ZAF/PROZA correction software supplied by Noran (Bastin and Heijligers 1991). The total amount of oxides and Cl in each analysis varied between 1.0 and 19 wt% with an average of 4.3 wt% for all 165 analyzed HDF microinclusions and between 1.9 and 90 wt% with an average of 12.5 wt% for 117 analyzed mineral microinclusions (Supplementary File 1, 2 - Table S1, S2). The low and variable sums reflect the small size of the inclusions, their depth and their high content of undetected water and carbonates. Precision approximately follows: 2σ (%) = 2/oxide in wt% (Jablon and Navon 2016), and is <20% for oxide concentrations of 0.05 wt%, <10% for 0.25 wt%, <6% for 0.5 wt% and < 2% for 1 wt%. The ZAF/PROZA processing assumed that the difference from 100 wt% is comprised of pure carbon. Later, all oxide and chlorine concentrations were normalized to 100 wt% on a carbon-free and volatiles-free basis (where Cl is present, excess calculated oxygen leads to a normalized total of more than 100%) and the average composition of the HDF in the diamond was calculated.

Laser ablation inductively coupled plasma mass spectrometry (LA-ICP-MS) analyses

Trace element concentrations were determined using a Quantel Brilliant 266 nm Nd:YAG pulsed laser with a beam diameter of 100 μm coupled to an Agilent 7500 ICP-MS. Background was measured for 100 s followed by 130 s of diamond ablation. Data were reduced using the GLITTER 4.4 software (Griffin et al. 2008). A doped cellulose external standard and the diamond carbon as internal standard were used (Rege et al. 2010; Rege et al. 2005). Only the most homogeneous and stable portions of the time-resolved signals were selected for each diamond. For the high impurity content of the diamond, blank corrections (Rege et al. 2005) are less than 1–2%, except for Ca where it is equivalent to 12 ± 5 ppm or 10% of the typical measured concentrations. The method limit of detection (LOD) is defined as 3.25 times the uncertainty on the background counts and the limit of quantitation (LOQ) is defined as 10 times the uncertainty on the background (Rege et al. 2010). The precision (expressed as %rsd) is 10% for concentrations between 1 and 100 ppm, 20% for 0.1–1 ppm, 30% for 0.01–0.1 ppm and 40% for values <0.01 ppm. These analyses yield the concentrations of elements in the diamond host. In order to obtain the trace element concentrations of the trapped fluids, all values were corrected to the average K content of the microinclusions of each diamond as measured by EPMA (on a water+carbonate free basis).

Results

Interstitial impurities and microinclusions' infrared absorbance

Two diamond populations are observed within the analyzed Finsch samples, based on their nitrogen concentrations and aggregation state. Three diamonds (ON-FCH-351, 352 and 355) carry 100 to 400 ppm nitrogen and exhibit absorption due to nitrogen in A-centers exclusively (pure Type IaA spectrum; Fig. 2 and Table 1). The other 4 diamonds (ON-FCH-349, 350, 354 and 356) have nitrogen concentrations between 500 to 1400 ppm and show absorption of both A- and B-centers (Type IaAB spectrum), with 25–35% of their nitrogen residing in B-centers. They have an associated platelet band at

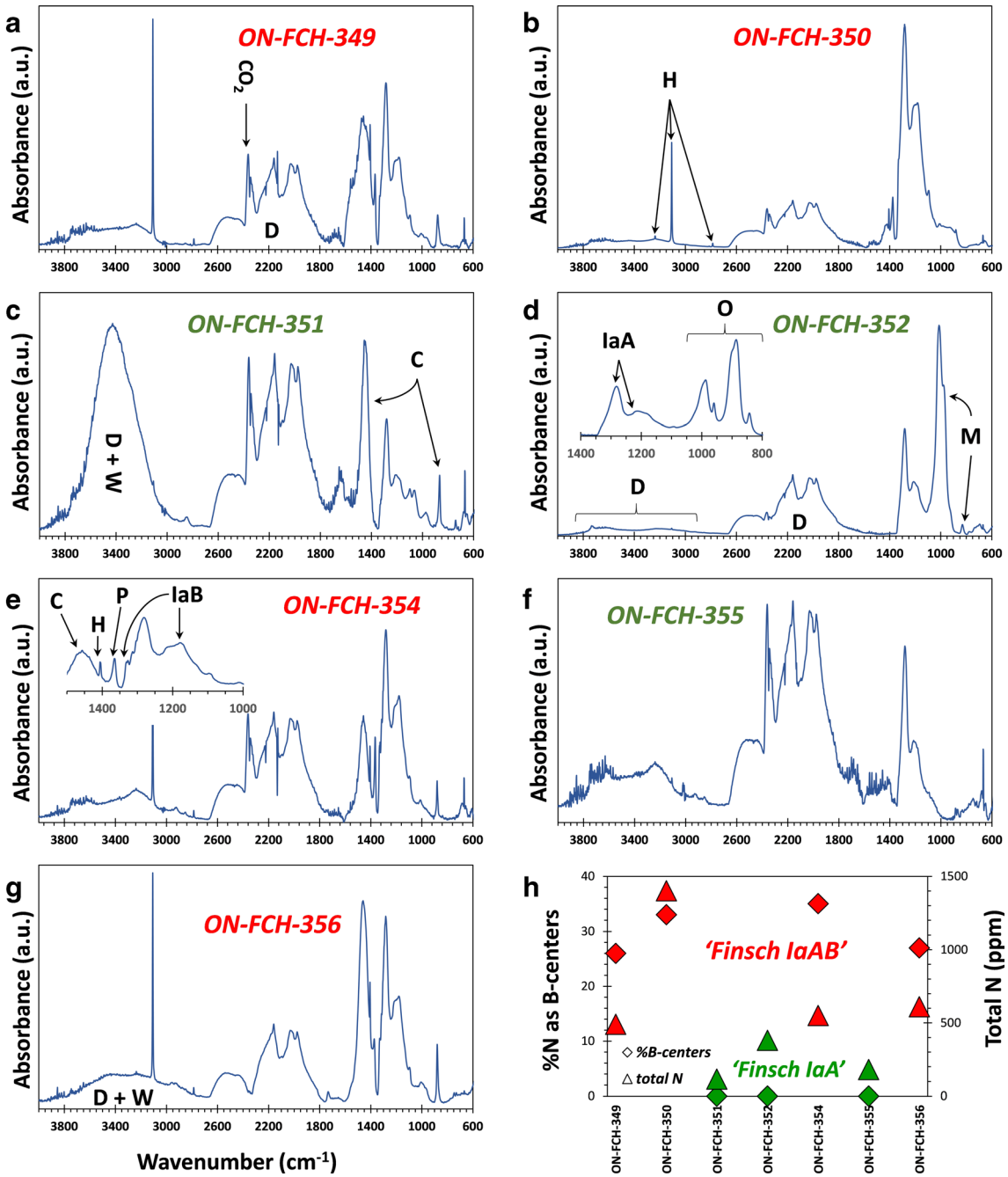

Fig. 2 Original infrared absorbance spectra of seven microinclusion-bearing diamonds from the Finsch Group II kimberlites (**a-g**). The intrinsic diamond bands at 1800–3800 cm^{-1} (**D**), without CO_2 and water overlapping absorbance, is best shown in (**d**). Nitrogen-related substitutions (**IaA** and **IaB**) in the diamond lattice show absorbance in the rage of 1150–1400 cm^{-1}; diamonds ON-FCH-351, 352 and 355 (c, d and f) show nitrogen absorbance due to A-centers only (Type IaA spectrum; 'Finsch IaA' diamond population – labels in green); diamond ON-FCH-349, 350, 354 and 356 (**a, b, e, g**) show absorbance of both A- and B-centers (Type IaB spectrum; 'Finsch IaAB' population – labels in red), nitrogen platelets peak (**P**; 1373 cm^{-1}) and hydrogen-related peaks (**H**; C-H vibration in a VN_3H center; 1405, 2785, 3107 and 3237 cm^{-1}). Absorbance due to mineral microinclusions and daughter phased within HDF microinclusions are also observed: bands at ~1450 and ~880 and ~750 cm^{-1} are typical of carbonate absorption (**C**). The broad band at ~3440 cm^{-1} and the peak at ~1650 are due to the presence of liquid water (**W**). In (**d**), strong absorption of mica (**M**; central peak at ~1010 cm^{-1}) microinclusions is observed in different parts of diamond ON-FCH-352; the inset in (**d**) shows the absorbance due to olivine (**O**) microinclusions in other parts of this diamond (absorbance due to HDF microinclusions is not observed in this diamond). (**h**) total nitrogen (ppm) and %N as B-centers in 'Finsch IaA' (green symbols) and 'Finsch IaAB' (yellow symbols) diamond populations

1373 cm^{-1} and pronounced hydrogen-related peaks (C-H vibration in a VN_3H center) at 1405, 2785, 3107 and 3237 cm^{-1} (Fig. 2). For distinguishing between the two groups of diamonds, we will use the term 'Finsch IaA' and 'Finsch IaAB' throughout this paper.

Infrared absorbance due to primary mineral microinclusions and/or HDF microinclusions (including various daughter mineral phases and a residual low-density hydrous solution) is observed for all diamonds. The absorbance of water (IR bands center at ~3440 and 1650 cm^{-1}) and carbonate (~1450 and 880 cm^{-1}) is found in both 'Finsch IaA' and 'Finsch IaAB' diamonds. However, the ratio of these two phases, expressed as the molar ratio of carbonate/(carbonate+water) (CMF), is different for the two diamond groups: varying between CMF = 0.10–0.13 in 'Finsch IaA' and between 0.43–0.51 in 'Finsch IaAB' diamonds (Table 1). A band/shoulder at ~1000 cm^{-1} and a small peak at 605 cm^{-1} in some of the spectra collected, is due to the presence of mica and apatite daughter phases in the HDF microinclusions, respectively. Additional silicate absorption peaks in the range between 800 and 1150 cm^{-1} are observed in diamonds ON-FCH-349, 350 and 351 (Fig. 2); however, clear mineral identification based on spectral features could not be achieved. No carbonate or water bands were detected in diamond ON-FCH-352 (Fig. 2), suggesting the lack of, or very small amount of HDF microinclusions in this specific diamond. Strong absorbance by both mica (central peak at ~1010 cm^{-1}, a shoulder at 975, and a minor peak at 831 cm^{-1}) and olivine (~989, 960, 887 and 843 cm^{-1}) is observed in different regions of this diamond (in agreement with EPMA data below).

Microinclusions' major- and trace-element compositions

General remarks

One hundred and sixty-five HDF microinclusions and 117 mineral microinclusions were analyzed in the inclusion-rich zones of the seven diamonds from Finsch (Figs. 1 and 3). The nitrogen-based distinction between two diamond populations is further observed in their HDF microinclusion compositions: 'Finsch IaA' diamonds are rich in saline HDFs (ON-FCH-351 and 355), while 'Finsch IaAB' diamonds contain high-Mg carbonatite (ON-FCH-349, 354 and 356) or 'low-Mg carbonatite-like' (ON-FCH-350) compositions. Variations between individual diamonds, and between saline and carbonatite HDFs, are described below. The average major-element composition of the HDFs and mineral microinclusions and trace element analyses in each diamond are presented in Tables 1, 2 and 3, respectively. Raw data for individual microinclusion analyses are tabulated in Supplementary File 1 and 2 - Table S1 and S2; trace element analyses are in Supplementary File 3 - Table S3.

Saline HDFs

HDF microinclusions in two of the 'Finsch IaA' diamonds (ON-FCH-351 and 355; 0% B-centers) show similar saline compositions, that fall close to the saline HDF end-member when projected on a $SiO_2 + Al_2O_3$–$CaO + MgO + FeO$–$Na_2O + K_2O$ or a Cl–$CaO + MgO + FeO$–$Na_2O + K_2O$ ternary diagram (Fig. 3a,b). The average major element compositions of the saline HDFs in diamond ON-FCH-351 and ON-FCH-355 overlap within error (1σ), however in general the composition of the latter one is higher in K_2O and CaO, and lower in Cl, FeO and Na_2O (Fig. 4). In both diamonds the HDF microinclusions span a limited range of compositions, lacking any core-to-rim compositional evolution. The HDF molar K/Cl and (K + Na)/Cl ratios in diamond ON-FCH-351 are 0.71 ± 0.16 (1σ) and 1.12 ± 0.44, respectively, while in ON-FCH-355 K/Cl = 1.28 ± 0.17 and (K + Na)/Cl = 1.67 ± 0.34.

The average saline HDF (on a carbonate and water free basis) has Cl = 30.8 ± 7.2 wt% (1σ = STDEV), K_2O = 38.5 ± 6.5 wt% and Na_2O = 9.8 ± 2.5 wt%. Other major oxides make up about 28 wt% altogether: SiO_2 = 5.0 ± 0.2, CaO = 4.6 ± 2.0, MgO = 1.7 ± 0.6, FeO = 11.5 ± 3.2, BaO = 1.4 ± 0.8, Al_2O_3 = 1.3 ± 0.2, P_2O_5 = 1.4 ± 0.7 and TiO_2 = 0.9 ± 0.3 wt% (as these saline fluids carry Cl^- as a major anion, the total Cl + oxides sum up to >100% due to excess calculated oxygen). Following Weiss et al. (2018), we estimate the molar proportions of carbonate (and CO_2) in the saline HDF as CO_3 = Mg + Fe + Ca + Ba+(Na + K-Cl-Si/3)/2-5P/3-(Si-2 × Ti-(Al-Si/3) × 3/2); assuming cations with positive charge in the fluid are balanced by either carbonate, chloride, phosphate or silicate ions (silicate phase is assumed to be mica). Once the CO_2 is calculated, the water content is determined based on the FTIR CMF ratio (Table 1). When both water and carbonate are included and the total is re-normalized to 1 kg of water (55.5 mol), the saline HDFs have an average molal proportion of: $Si_{1.9}Ti_{0.3}Al_{0.6}Fe_{3.7}Mg_{1.0}Ca_{1.9}Ba_{0.2}Na_{7.3}K_{18.8}P_{0.5}Cl_{20.0}(CO2)_{7.2}(H_2O)_{55.5}$. Assuming that the main components of the saline HDFs are water, chlorides, carbonates, phosphates and silicates, chlorides make up 40% by weight, carbonates – 21%, silicates – 9%, phosphates – 2% and water make up 28% of the HDFs.

Trace-element patterns of HDF in ON-FCH-351 and ON-FCH-355 are very similar (Fig. 5a). They are characterized by elevated concentrations of incompatible elements, with the most incompatible elements (Cs–Pr) reaching levels of a few hundred to a few thousand times the primitive mantle (PM) values. Ba, Th, U, alkalis (K, Rb and Cs) and LREEs are similarly enriched and elevated compared to Nb and Ta levels; Ti, Zr and Y show characteristic negative anomalies.

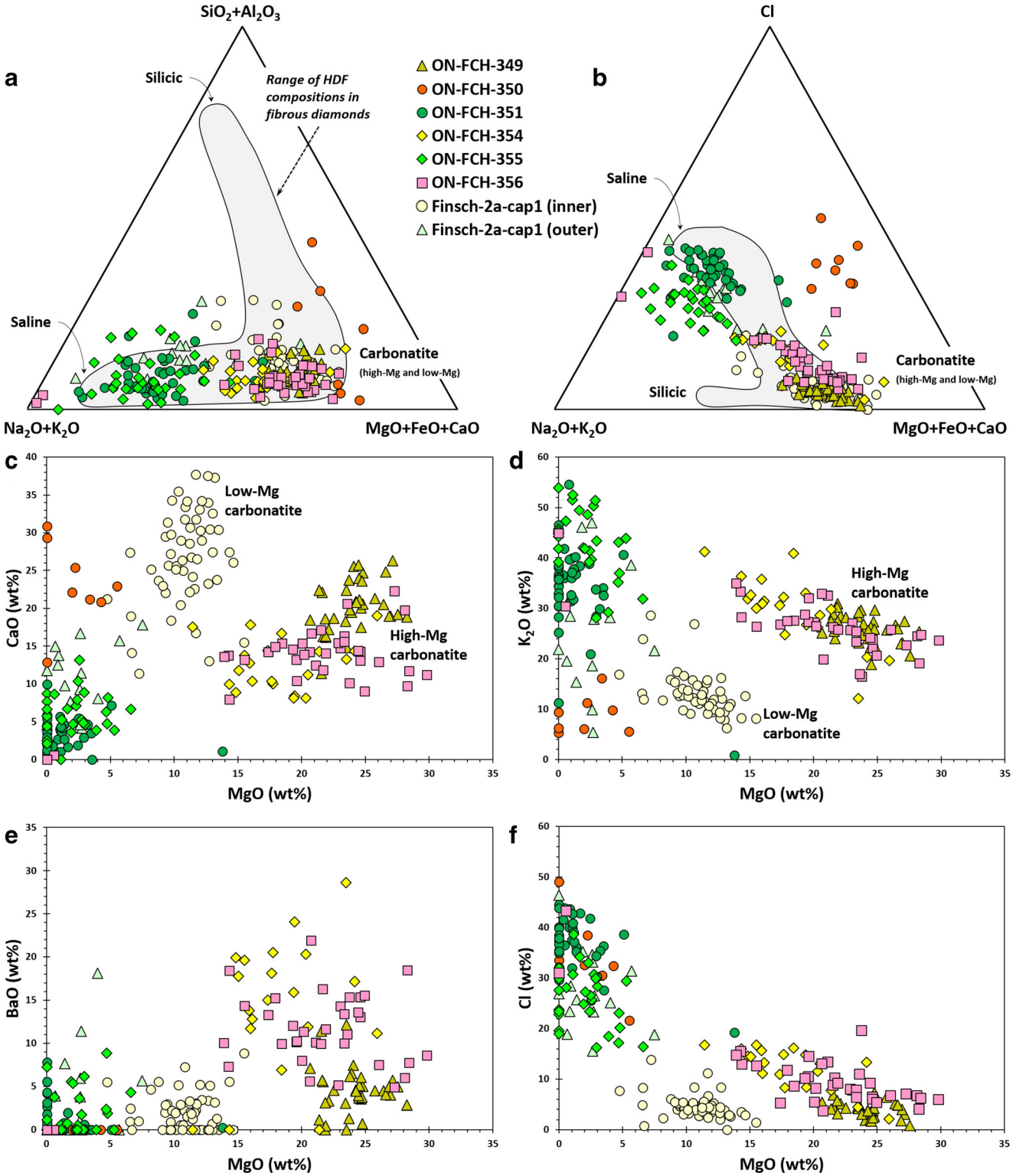

Carbonatite HDFs

Three diamonds of the 'Finsch IaAB' population (ON-FCH-349, 354 and 356; 26–35% B-centers) carry high-Mg carbonatite HDF microinclusions, with MgO varying between 15 to 30 wt% (Fig. 3c-f). HDFs in diamond ON-FCH-354 have higher BaO, K_2O and Cl, and lower MgO, FeO, CaO and Na_2O compared to compositions in diamond ON-FCH-349, while microinclusions in ON-FCH-356 span the full compositional range covered by ON-FCH-349 and ON-FCH-354 microinclusions. Intra-diamond variations exist: MgO correlates negatively with Cl and K_2O (which show

◀ **Fig. 3** Compositions of HDF microinclusions in diamonds from the Finsch Group II kimberlite (all plots are in wt%). (**a**) $SiO_2 + Al_2O_3$–$Na_2O + K_2O$–MgO + FeO + CaO ternary diagram, and (**b**) Cl–$Na_2O + K_2O$–MgO + FeO + CaO ternary diagram, showing the HDFs composition in Finsch diamonds compared to the global compositional HDF end-members varying between saline to silicic to carbonatite (shaded area, delineated by average compositions for 90 individual diamonds). High-Mg and low-Mg carbonatite end-members plot together in both ternary diagrams, but variations between these two end-members can be seen in plots (**c**) to (**f**). (**c-f**) Oxides vs. MgO variations, showing differences between 'Finsch IaA' diamonds carrying saline HDFs and 'Finsch IaAB' diamonds carrying high-Mg carbonatitic and 'low-Mg carbonatite-like' compositions (see text for more info); some differences also occur between diamonds of the same group. Also shown, the compositions of microinclusions found in two different growth layers along the rim of a monocrystalline diamond from Finsch (Finsch_2a_cap1 (inner) – low-Mg carbonatite, Finsch_2a_cap1 (outer) – saline; Weiss et al. 2014)

positive correlations between them) in both ON-FCH-354 and ON-FCH-356 (Fig. 3d,f), limited correlations between MgO–FeO and MgO–SiO_2 are also observed (not shown). In diamond ON-FCH-356 Cl, Na_2O and K_2O correlate positively. On a carbonate and water free basis, the average high-Mg carbonatite HDF has MgO = 21.4 ± 3.0 wt% (1σ = STDEV), CaO = 15.6 ± 4.1 wt% and K_2O = 27.2 ± 2.3 wt%. Other major oxides make up about 30 wt%: SiO_2 = 6.0 ± 1.4, FeO = 6.7 ± 0.9, BaO = 10.1 ± 5.1 and Cl = 8.5 ± 4.1 wt%. TiO_2, Al_2O_3, Na_2O and P_2O_5 make up 6.5 wt% altogether. The result of Cl^- being a major anion in these high-Mg HDFs, the total Cl + oxides sum up to ~102% due to excess calculated oxygen. For high-Mg compositions, we estimated the molar proportions of carbonate (and CO_2) as CO_3 = Mg + Fe + Ca + Ba+Na/2 + K/2 + 2Ti-Cl/2-5P/3-(5Si + 9Al)/8-(Si + Al)/

Table 2 Major-element composition and calculated mineral formulae of microinclusions in Finsch diamonds

Diamond	ON-FCH-349	ON-FCH-350	ON-FCH-351	ON-FCH-352	
Mineral phase	Orthopyroxene	Clinopyroxene	Clinopyroxene	Olivine	Phlogopite
Number of inclusions analyzed	18	37	11	16	34
EPMA results (wt%)					
SiO_2[a]	60.7 (4.3)	52.4 (4.4)	54.2 (1.5)	42.8 (1.4)	47.0 (2.9)
TiO_2	0.2 (0.3)	0.5 (0.9)	0.2 (0.3)	0.0 (0.1)	0.8 (0.8)
Al_2O_3	3.7 (2.6)	6.4 (1.0)	8.0 (1.1)	0.5 (0.5)	12.9 (1.1)
Cr_2O_3	–	–	0.2 (0.3)	0.3 (0.5)	0.7 (0.8)
FeO	4.2 (1.8)	4.8 (1.5)	6.8 (2.0)	7.7 (1.6)	2.9 (1.4)
MgO	27.7 (3.6)	11.1 (1.3)	10.7 (1.5)	47.1 (1.7)	25.0 (1.8)
CaO	1.1 (0.6)	16.9 (1.5)	11.2 (1.4)	0.3 (0.4)	0.4 (0.5)
BaO	0.9 (1.8)	0.5 (0.9)	0.1 (0.3)	0.2 (0.3)	0.1 (0.2)
Na_2O	0.8 (0.7)	5.0 (1.1)	6.7 (2.0)	0.4 (0.6)	0.6 (0.9)
K_2O	0.4 (0.7)	0.5 (0.7)	0.6 (0.9)	0.2 (0.2)	8.7 (3.0)
P_2O_5	0.2 (0.4)	0.3 (0.5)	0.7 (1.4)	0.4 (1.0)	0.5 (0.8)
Cl	0.1 (0.2)	2.1 (3.4)	0.7 (1.0)	0.2 (0.3)	0.4 (0.5)
Total[b]	10.6 (5.3)	9.7 (8.5)	9.7 (6.4)	12.7 (20.3)	16.9 (25.5)
Mg#[c]	0.92 (0.03)	0.81 (0.06)	0.74 (0.07)	0.92 (0.02)	0.94 (0.03)
Calculated mineral formulae (apfu)[d]					
Si[e]	2.08 (0.10)	1.95 (0.07)	1.99 (0.03)	1.04 (0.03)	3.41 (0.15)
Ti	0.00 (0.01)	0.01 (0.03)	0.01 (0.01)	0.00 (0.00)	0.05 (0.05)
Al	0.15 (0.11)	0.28 (0.04)	0.35 (0.05)	0.01 (0.01)	1.11 (0.10)
Cr	–	–	0.01 (0.01)	0.01 (0.01)	0.04 (0.05)
Fe	0.12 (0.05)	0.15 (0.05)	0.21 (0.06)	0.16 (0.03)	0.18 (0.08)
Mg	1.42 (0.21)	0.62 (0.07)	0.58 (0.07)	1.71 (0.05)	2.71 (0.17)
Ca	0.04 (0.02)	0.68 (0.09)	0.44 (0.05)	0.01 (0.01)	0.03 (0.04)
Na	0.01 (0.01)	0.09 (0.02)	0.12 (0.04)	0.00 (0.01)	0.02 (0.03)
K	0.00 (0.01)	0.01 (0.01)	0.01 (0.01)	0.00 (0.00)	0.20 (0.07)
Σ of cations	3.83 (0.09)	3.79 (0.05)	3.70 (0.05)	2.94 (0.03)	7.74 (0.09)

[a] Oxide average in wt% after normalization (water and carbonate free basis), and its standard deviation (1σ).

[b] Initial analytical totals of oxides and Cl (wt%) before normalization

[c] Mg# = 100 × Mg/(Mg + Fe) molar ratio

[d] Calculated on the basis of 6 (opx, cpx), 4 (ol) and 12 (phl) oxygen atoms per formula unit

[e] Cation average and its standard deviation

Table 3 Trace elements compositions in Finsch Diamonds

Sample	ON-FCH-349	ON-FCH-350	ON-FCH-351	ON-FCH-352	ON-FCH-354	ON-FCH-355	ON-FCH-356
K_2O (wt%)[a]	26.0	8.7	34.0		29.8	43.1	25.8
No. of analyses[b]	6	2	4	5	2	5	5
Element (ppm) [c]							
Cs	0.049 (0.003)	0.054 (0.005)	0.056 (0.007)	0.010 (0.002)	0.13 (0.02)	0.023 (0.003)	0.09 (0.01)
Rb	0.49 (0.03)	1.8 (0.2)	1.8 (0.2)	0.8 (0.1)	1.0 (0.2)	0.69 (0.06)	0.74 (0.05)
Ba	43 (5)	19 (3)	27 (5)	0.75 (0.06)	263 (25)	17.6 (1.0)	128 (6)
Th	0.062 (0.008)	0.047 (0.008)	0.30 (0.06)	0.010 (0.001)	3.2 (0.2)	0.15 (0.01)	0.71 (0.03)
U	0.037 (0.005)	0.007 (0.002)	0.06 (0.01)	0.003 (0.001)	0.76 (0.04)	0.026 (0.003)	0.16 (0.01)
K	264 (9)	31 (2)	533 (51)	134 (13)	495 (64)	264 (32)	378 (33)
Ta	0.006 (0.002)	0.008 (0.002)	0.007 (0.003)	0.012 (0.002)	0.003 (0.001)	0.009 (0.002)	0.008 (0.002)
Nb	0.14 (0.02)	0.044 (0.008)	0.30 (0.06)	0.080 (0.005)	0.26 (0.01)	0.28 (0.01)	0.133 (0.008)
La	0.31 (0.02)	0.20 (0.03)	0.84 (0.15)	0.005 (0.001)	8.7 (0.4)	0.80 (0.04)	2.27 (0.08)
Ce	0.76 (0.06)	0.32 (0.04)	0.6 (0.1)	0.006 (0.001)	15.2 (0.6)	0.85 (0.04)	3.7 (0.2)
Pr	0.17 (0.02)	0.046 (0.006)	0.05 (0.01)	0.002 (0.001)	1.70 (0.09)	0.077 (0.005)	0.44 (0.02)
Sr	2.8 (0.1)	1.8 (0.2)	7.8 (1.1)	0.058 (0.004)	43 (2.5)	4.0 (0.2)	16.5 (0.6)
Nd	1.1 (0.1)	0.17 (0.03)	0.15 (0.03)	0.03 (0.01)	4.2 (0.2)	0.20 (0.03)	1.19 (0.08)
Sm	0.09 (0.01)	0.04 (0.01)		0.012 (0.006)	0.10 (0.01)	0.03 (0.01)	0.04 (0.01)
Hf	0.011 (0.004)	0.016 (0.005)	0.009 (0.005)	0.016 (0.003)			0.009 (0.005)
Zr	0.23 (0.02)	0.041 (0.007)	0.025 (0.006)	0.016 (0.003)	0.11 (0.01)	0.091 (0.007)	0.056 (0.006)
Eu	0.011 (0.002)	0.020 (0.003)		0.008 (0.002)	0.015 (0.002)	0.014 (0.003)	0.011 (0.003)
Ti	3.0 (0.2)	1.6 (0.2)	1.2 (0.3)	5.7 (0.3)	0.26 (0.05)	2.2 (0.15)	0.19 (0.07)
Gd	0.026 (0.007)		0.012 (0.009)	0.027 (0.005)	0.044 (0.007)		0.025 (0.009)
Dy	0.017 (0.004)	0.013 (0.005)	0.015 (0.005)	0.007 (0.003)		0.009 (0.005)	0.011 (0.005)
Y	0.037 (0.003)	0.035 (0.003)	0.006 (0.002)	0.002 (0.001)	0.004 (0.001)	0.008 (0.002)	0.008 (0.002)
Ho	0.004 (0.001)	0.006 (0.002)	0.002 (0.001)	0.001 (0.001)		0.003 (0.001)	0.003 (0.001)
Er	0.019 (0.004)		0.009 (0.006)	0.014 (0.004)		0.019 (0.005)	
Yb	0.010 (0.006)		0.016 (0.006)	0.008 (0.004)		0.021 (0.008)	
Lu	0.003 (0.001)	0.004 (0.001)		0.004 (0.001)	0.002 (0.001)	0.006 (0.001)	0.005 (0.001)

[a] K_2O content (wt%) of the HDFs as measured by EPMA

[b] The number of LA-ICP-MS analyses that were included in the average

[c] All values as measured by LA-ICP-MS in the diamond after blank correction and before normalization to the K content of the microinclusions based on EPMA, Standard deviations are quoted in brackets and includes counting statistics on the integrated number of counts for each element and for the carbon internal standard, as well as errors due to the inhomogeneity of the cellulose standard

Empty cell = value below minimum detection limit

8 (assuming positive charged cations are balanced by either carbonate, chloride, phosphate or silicate ions; Klein-BenDavid et al. 2009), and calculated the water content based on the diamond FTIR CMF ratio (Table 1). When both water and carbonate are included and the total is re-normalized to 1 kg of water (55.5 mol), the high-Mg carbonatite HDFs have an average molal proportion of: $Si_{4.8}Ti_{0.9}Al_{1.1}Fe_{4.4}Mg_{25.3}Ca_{13.3}Ba_{3.1}Na_{3.1}K_{22.5}P_{1.2}Cl_{11.4}(CO2)_{50.6}(H_2O)_{55.5}$. Assuming that the main components of the high-Mg carbonatite HDFs are carbonates, water, silicates, chlorides and phosphates, Cl is entirely associated with K as KCl and the main silicate phase is mica, carbonates make up 68% by weight, chlorides – 11%, silicates – 7%, phosphates – 2% and water make up 13% of the HDF inclusions.

The trace-element pattern of high-Mg carbonatite HDFs in ON-FCH-354 is the most enriched among 'Finsch IaAB' diamonds (Fig. 5b). It shows highly elevated Ba, U and Th (~20,000 × PM values) and LREEs, relative depleted alkalis (K, Rb and Cs), Nb and Ta, and negative anomalies of Sr, Ti, Zr, Hf and Y relative to REEs of similar compatibility. The patterns in diamond ON-FCH-356 and ON-FCH-349 are somewhat different. Changes are observed in trace element ratios, and follow variations in the average major element carbonatitic composition (Fig. 6a-i): the enrichment of LREEs over heavier REEs (e.g. La/Gd) decreases with increasing MgO and CaO, and decreasing Cl content. Th/Nb, Sr/Rb, Gd/Ti and Gd/Y ratios show similar behavior, while Ba/U and Ba/La ratios increase with increasing MgO and CaO.

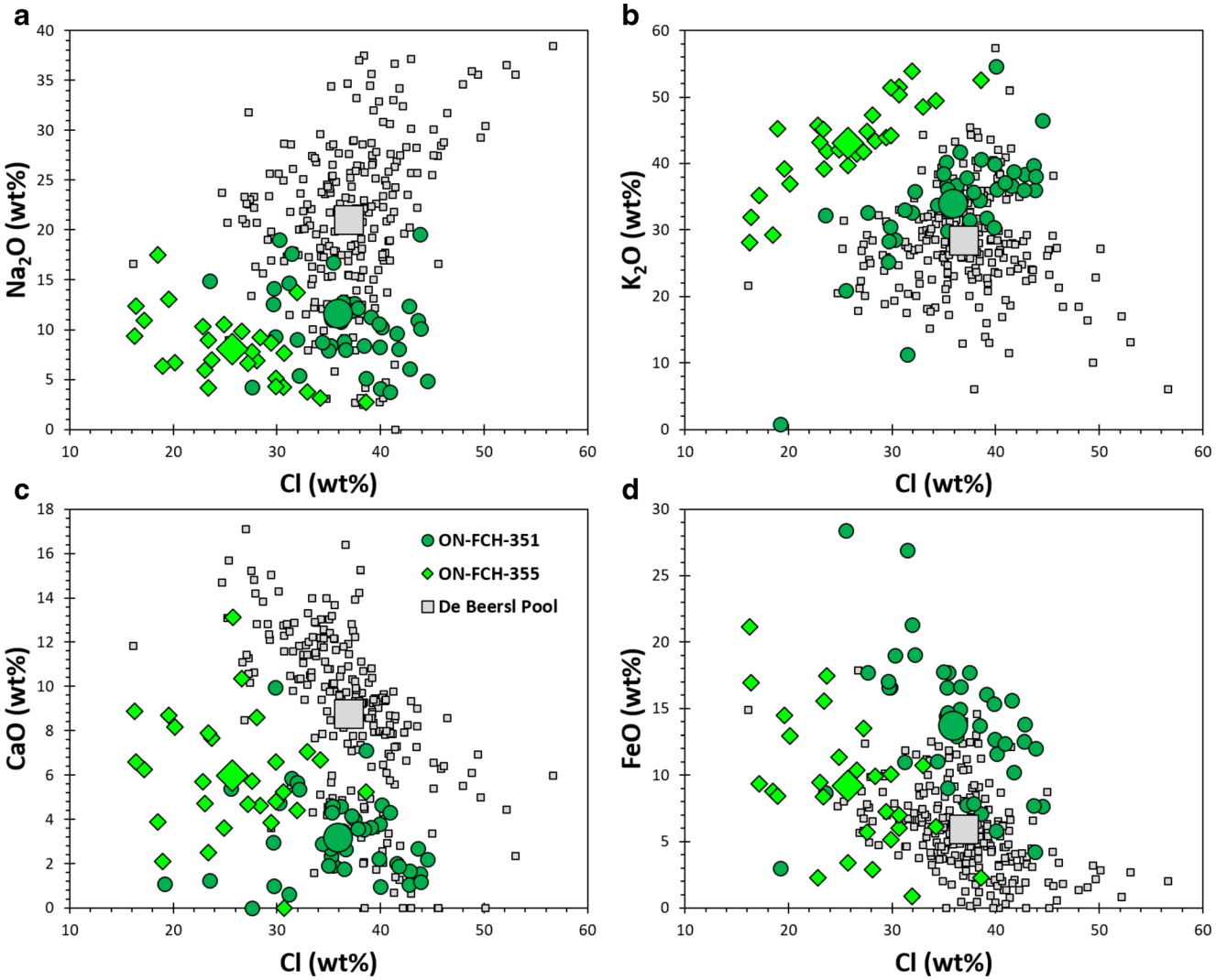

Fig. 4 Compositions of saline HDF microinclusions in diamond from the Finsch Group II kimberlite (ON-FCH-351 and ON-FCH-355). (**a-d**) Oxides vs. Cl content (all plots are in wt%). Also shown, the compositions of saline HDF microinclusions in diamonds from the De Beers Pool Group I kimberlites (Weiss et al. 2018). In all plots, small symbols – individual inclusions, large symbols – average compositions

Diamond ON-FCH-350, with 33% B-centers, is part of the 'Finsch IaAB' diamonds population. Eight microinclusions with an average composition of CaO = 23.2 ± 5.6 wt%, FeO = 16.2 ± 6.1, SiO_2 = 11.4 ± 9.9, K_2O = 8.7 ± 3.7, Na_2O = 5.6 ± 3.6, Cl = 34.4 ± .8 and TiO_2, Al_2O_3, MgO and P_2O_5 which make up ~8 wt% altogether, were found in this diamond. The FTIR absorbance of water and carbonate in this diamond is small (Fig. 2b), but it suggests that these micoinclusions contain HDFs. The HDF in ON-FCH-350 has similar CaO and K_2O contents to low-Mg carbonatite HDF found in microinclusions in an octahedral diamond from Finsch (Fig. 3c,d; Weiss et al. 2014), but it is lower in MgO and contains significantly higher amount of Cl (Fig. 3b,f). Based on the high CaO + MgO + FeO (~42 wt%) and the presence of carbonate, we consider the HDF in diamond ON-FCH-350 to be carbonatite ('low-Mg carbonatite-like') and that Ca, as the main cation, compensates for some of the high amount of Cl.

The trace element pattern of diamond ON-FCH-350 is mostly flat with no significant elemental anomalies and a moderate decrease in concentrations from the most incompatible elements toward the more compatible ones (Fig. 5b). Based on EPMA analyses, the majority of microinclusions in this diamond are omphacite and only eight HDF microinclusions were found (Fig. 1). Therefore, LA-ICP-MS analyses likely average omphacite±HDF microinclusions, and the trace element pattern observed for diamond ON-FCH-350 represents metasomatised omphacite, or the average of a mixture between mostly omphacite and some HDF microinclusions.

Mineral microinclusions

Omphacite microinclusions are found in ON-FCH-350 and ON-FCH-351, of the 'Finsch IaAB' and 'Finsch IaA'

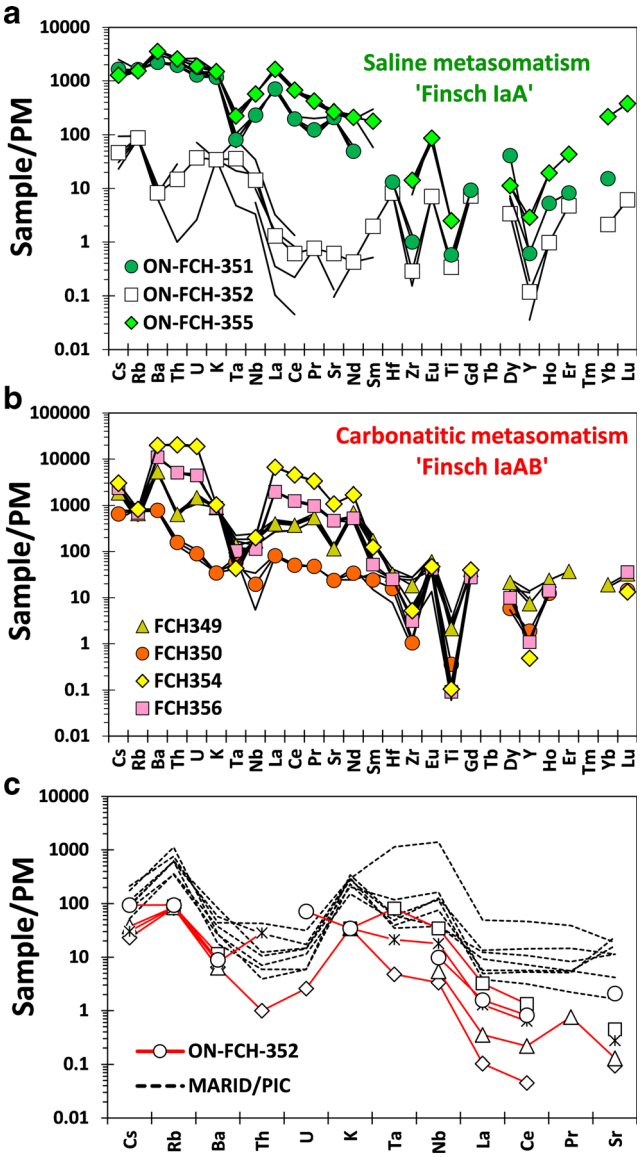

Fig. 5 Primitive-mantle-normalized incompatible-element patterns of HDFs trapped in Finsch diamonds. (**a**) 'Finsch IaA' diamonds – ON-FCH-351 and 355 carry saline HDFs; ON-FCH-352 carries phlogopite and olivine microinclusions, no HDF microinclusions were found in this diamond. (**b**) Finsch IaAB' diamonds – ON-FCH-349, 354 and 356 carry high-Mg carbonatite HDFs, in ON-FCH-349 HDFs are associated orthopyroxene microinclusions; ON-FCH-350 carries omphacite microinclusions, few microinclusions of 'low-Mg carbonatite-like' compositions were identified by EPMA (see text for details). (**c**) Presents the similarity in trace elements between phlogopite (±olivine) microinclusions in ON-FCH-352 and MARID and PIC xenoliths from the Kimberley area, South Africa. In (**a**) and (**b**), the HDF average composition in a single diamond is represented by patterns with symbols, individual LA-ICP-MS analyses are lines with no symbols; in (**c**), ON-FCH-352 patterns are individual LA-ICP-MS analyses in different parts of the diamond, MARID and PIC patterns are individual xenoliths. Primitive mantle values are from McDonough and Sun (1995)

diamonds, respectively. In diamond ON-FCH-351 these omphacites have an average composition corresponding to molar end-member proportions of $Aeg_{23}Di_{48}Jd_{29}$. The average Mg# [100 × Mg/(Mg + Fe) molar ratio] is 74 ± 7 (1σ = STDEV), TiO_2 = 0.2 ± 0.3 wt% and K_2O = 0.6 ± 0.9 wt%. Minor Cl (0.7 ± 1.0 wt% on average) was detected in few of the microinclusions, plausibly from traces of saline HDFs. Omphacites in diamond ON-FCH-350 are more diopside-rich, and have an average composition corresponding to molar end-member proportions of $Aeg_{14.5}Di_{65}Jd_{20.5}$. They have an average Mg# = 81 ± 6, TiO_2 = 0.5 ± 0.9 wt% and K_2O = 0.5 ± 0.7 wt%. Decreasing Si per formula units with increasing levels of Cl (up to 12 wt%; Fig. 7a), and increasing K and Na (not shown), indicate mixing between omphacite and HDFs in some of the microinclusions.

Olivine microinclusions in diamond ON-FCH-352, of the 'Finsch IaA' diamonds, have an average Mg# = 92 ± 2. The same diamond also contains phlogopite microinclusions, having an average Mg# = 94 ± 3, 13 ± 1 wt% Al_2O_3, 0.7 ± 0.8 wt% Cr_2O_3, 0.8 ± 0.8 wt% TiO_2 and a Si/Al and Si/(Al + Cr) cation ratio of 3.1 ± 0.4 and 3.0 ± 0.3, respectively. Small amounts of 0.6 ± 0.9 wt% Na_2O and 0.4 ± 0.5 wt% Cl were detected in these phlogopites, plausibly from traces of saline HDFs. The trace element pattern of microinclusions (olivine+phlogopite) in this diamond show great similarities in the most incompatible elements (Cs-Sr) to phlogopite-rich xenoliths (MARID and PIC) compositions (Fig. 5c; Grégoire et al. 2002), which is different compared to patterns of saline HDFs in 'Finsch IaA' diamonds (Fig. 5a).

Orthopyroxene microinclusions in diamond ON-FCH-349 have an average composition corresponding to an end-member composition of $En_{90}Fs_{7.5}Wo_{2.5}$, with Mg# = 92 ± 3, Al_2O_3 = 3.7 ± 2.6 and Na_2O = 0.8 ± 0.7 wt%. In most cases TiO_2 was not detected (Supplementary File 2 - Table S2).

Discussion and conclusions

Diamonds from the southwest Kaapvaal Craton date to ages as old as ~3 Ga (e.g. Pearson et al. 1998; Richardson et al. 1984; Smith et al. 1991; Aulbach et al. 2009). Considering the variations in nitrogen concentrations and aggregation state (up to 85% B-centers) between and within diamonds from Finsch, multiple episodes of diamond growth are revealed (Appleyard et al. 2004; Palot et al. 2013), throughout the Kaapvaal Craton history (e.g. Carlson et al. 2005; Pearson et al. 1995; Shirey et al. 2004; Simon et al. 2007). These diamond growth episodes were triggered by different metasomatic agents, as evidenced by δ^{13}C-N variations in octahedral and dodecahedral diamonds from Finsch (Palot et al. 2013), and by different types of HDFs (i.e. saline and low-Mg carbonatite compositions) included in two separate growth layers of an octahedral diamond from Finsch (Weiss et al. 2014). In the present study, two populations of microinclusion-bearing diamonds from the Finsch kimberlite have been identified based on their nitrogen aggregation state and the HDF type they encapsulated (Figs. 2

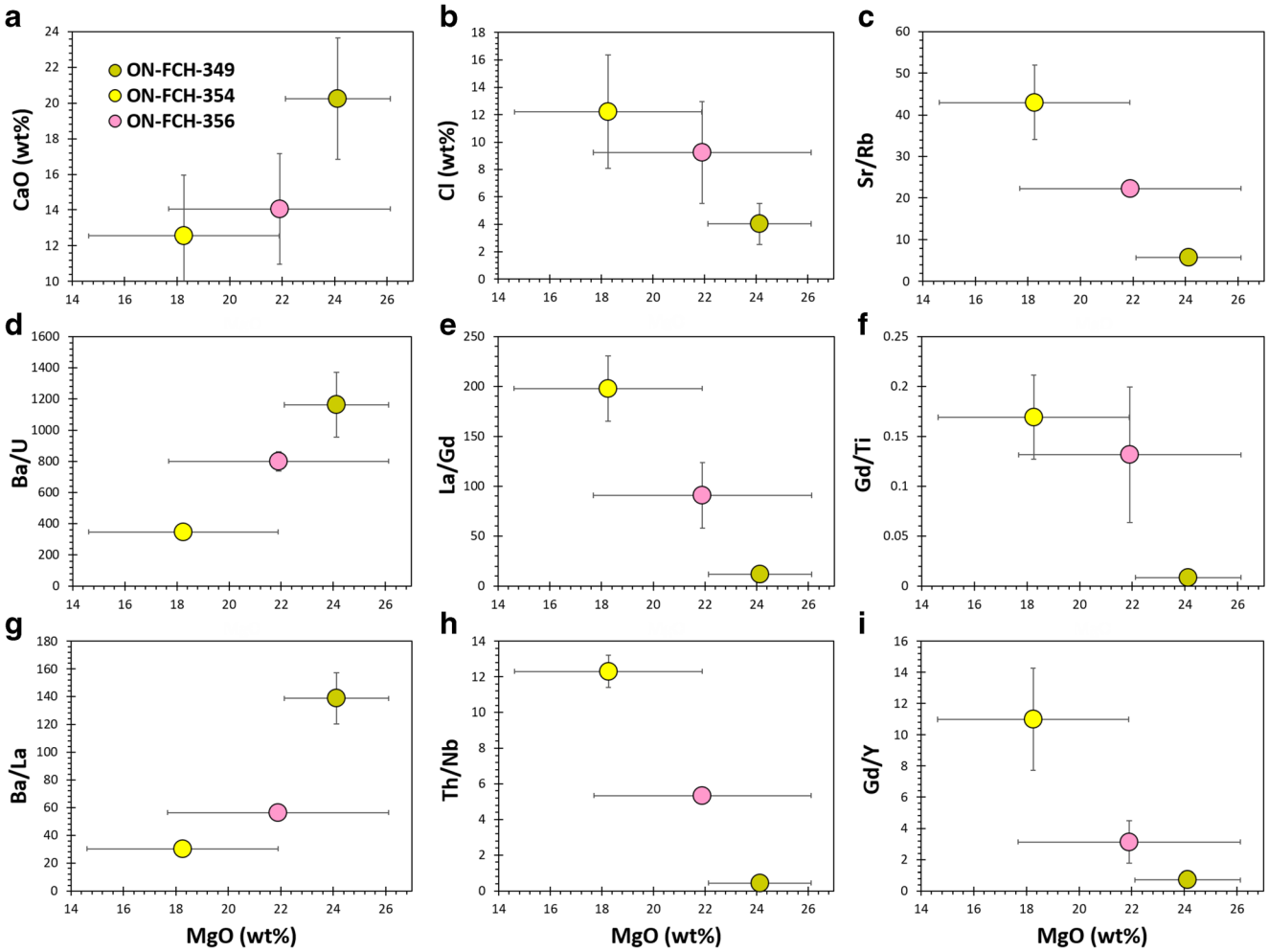

Fig. 6 Relationships between average MgO, CaO and Cl (**a,b**) and trace element ratios (**c-i**) in high-Mg carbonatite HDFs in 'Finsch IaAB' diamonds (ON-FCH-349, 354 and 356). MgO correlates positively with CaO, and both are negatively correlated with Cl contents (see also Fig. 3c,f). With increasing MgO and CaO, the enrichment of LILE (Ba, U, Th) and LREEs over the alkalis (K, Rb and Cs), Nb, Ta and the more compatible elements (especially compared to Ti, Zr and Y) decreases (i.e. lower La/Gd, Th/Nb, Sr/Rb, Gd/Ti and Gd/Y ratios). Ba/U and Ba/La ratios increase with increasing MgO and CaO, representing higher levels of enrichment of Ba compared to U, Th and the LREEs (see also incompatible-element patterns in Fig. 5b). We note that diamond ON-FCH-349 contains both high-Mg carbonatite HDFs and orthopyroxene microinclusions that were likely analyzed as a mixture during LA-ICP-MS measurements

and 3): 'Finsch IaA' diamonds have nitrogen solely in A-centers and contain saline HDF microinclusions, and 'Finsch IaAB' diamonds have nitrogen in both A- and B-centers (25–35% B-centers) and are characterized by carbonatitic HDFs (either high-Mg carbonatite or low-Mg carbonatite-like compositions).

Given the mantle residence temperatures (average temperature between diamond formation and when it ascended with the kimberlite) of 'Finsch IaA' and 'Finsch IaAB' diamonds, their nitrogen concentration and aggregation state can be used to provide temporal constraints on their formation, as well as on the metasomatic events in which the two populations of diamonds formed (Evans 1992; Taylor et al. 1990, 1996). We estimate the possible residence temperature for these diamonds to be between 1000 and 1250°C, based on thermobarometry results for non-diamondiferous and diamondiferous xenoliths and touching and non-touching inclusions in diamonds from Finsch and the neighboring kimberlites (Koffiefontein and De Beers Pool; Deines et al. 1984; Gurney et al. 1979; Phillips and Harris 1995; Rickard et al. 1989; Griffin et al. 1992; Izraeli et al. 2004; Lazarov et al. 2009; Phillips et al. 2004; Shee et al. 1982; Viljoen et al. 1992, 2014). Fig. 8a shows that "Finsch IaA' and 'Finsch IaAB' diamonds could have formed simultaneously, assuming residence temperature differences of 110–130°C for a minimum of ~20 Ma before the Finsch kimberlite erupted (at 118 Ma; Smith et al. 1985). This scenario is plausible if the two diamond populations formed at different depths, such as a 20–30 km difference along 38–40 mW/m^2 cratonic geotherms. On the other hand, the two populations of

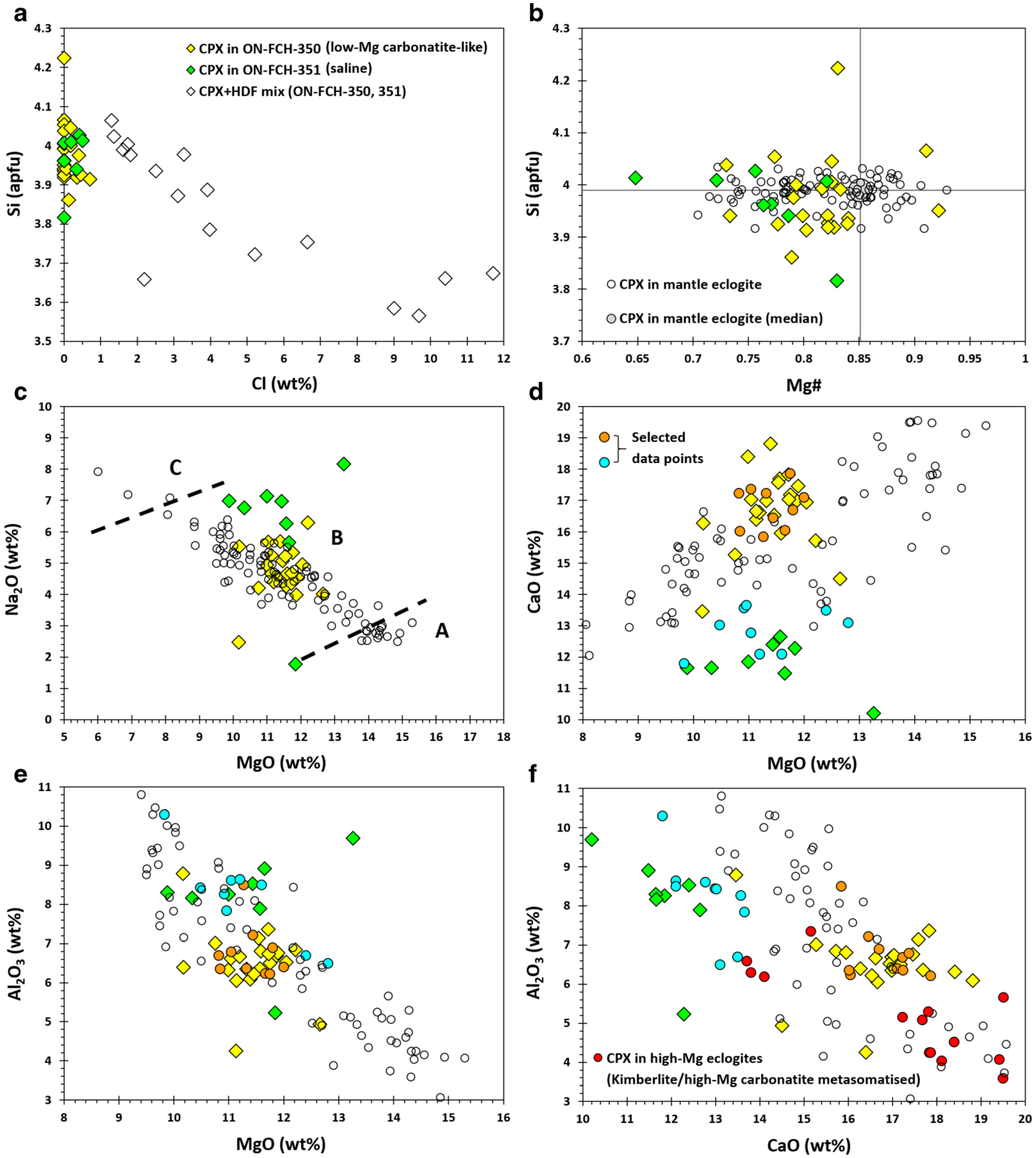

diamonds could have formed at different times (Fig. 8b). Assuming similar residence temperatures for both diamond groups, the minimum time gap between the formation of 'Finsch IaA' and 'Finsch IaAB' diamonds is ~15 Myr at 1250°C. This time difference grows longer with lower residence temperatures, up to ~1.5 Gyr at 1130°C; lower temperatures are unlikely as they require the formation of the 'Finsch IaAB' diamonds before 3 Ga. The time difference between the formation of the two diamond populations extends even longer, if the average residence temperature of 'Finsch IaA' diamonds was higher compared to 'Finsch IaAB' diamonds. We favor the formation of 'Finsch IaA' and 'Finsch IaAB' diamonds during two separate metasomatic events, as this scenario provides a simple explanation for both the nitrogen

◀ **Fig. 7** Compositions of omphacite microinclusions in association with saline HDFs (green diamonds, ON-FCH-351, 'Finsch IaA' diamonds) or low-Mg carbonatite-like HDF composition (yellow diamonds, ON-FCH-350, 'Finsch IaAB' diamonds, see text for details). Also shown are clinopyroxene compositions in mantle eclogite xenoliths (small open circles, Aulbach and Jacob 2016 and unpublished dataset). **(a)** Si atoms per formula unit (apfu) against Cl (wt%). Microinclusions containing mostly pure omphacite have low Cl content (Cl < 0.5 wt%) and cluster between Si = 3.9–4.1 pfu, while microinclusions containing a mixture of omphacite and HDF (open diamonds) show decreasing Si pfu with increasing Cl content (these are not shown in **b-f**). **(b)** Si pfu against Mg# (Mg/Mg + Fe molar ratio). Most omphacite microinclusions overlap the compositional range span by clinopyroxene in mantle eclogites. **(c)** Na_2O against MgO (wt%). Omphacite microinclusions in diamond ON-FCH-350 and ON-FCH-351, associated with either low-Mg carbonatite-like or saline HDFs, respectively, have MgO and Na_2O values that are classified into Group B eclogite, with the ones associated with saline HDFs having higher Na_2O at similar MgO values; A–B–C eclogite classification from Taylor and Neal (1989). **(d)** CaO against MgO (wt%), **(e)** Al_2O_3 against MgO (wt%) and **(f)** Al_2O_3 against CaO (wt%), show separation between omphacite associated with different HDF types. 'Selected data points' (blue and orange circles) were chosen from clinopyroxene-in-mantle-eclogites datasets to evaluate the possible relationship between omphacite composition and HDF type (see text for additional information). In (**f**), omphacites in high-Mg mantle eclogites, which were identified as metasomatised by kimberlite or high-Mg carbonatite are highlighted (red circles; Aulbach and Jacob 2016 and unpublished data). These mostly have high-CaO and low-Al_2O_3 values that are separated from omphacites associated with either saline or low-Mg carbonatitic-like HDFs

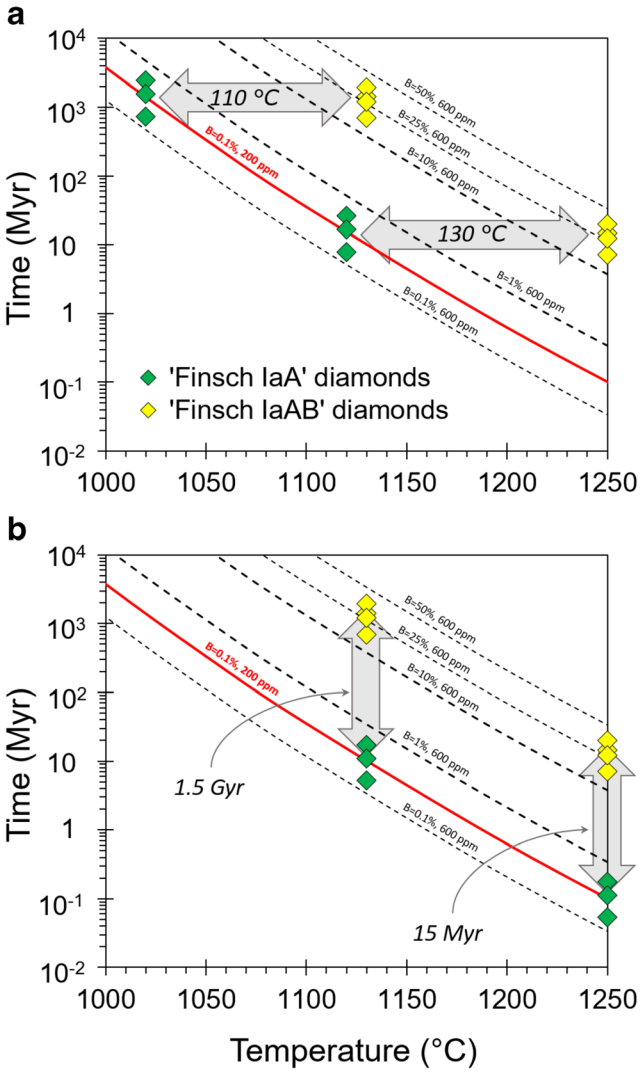

Fig. 8 The aggregation of nitrogen from A-centers (paired nitrogen atoms) to B-centers (aggregates of four nitrogen atoms) as a function of time and temperature, using the calibration of Taylor et al. (1990). The proportions of nitrogen in B-centers (%B) increase as nitrogen pairs aggregate to form larger aggregates of four atoms; %B calculated for total nitrogen of 600 ppm - dashed black contours, %B calculated for total nitrogen of 200 ppm – solid red contour. 'Finsch IaA' diamonds showing 'pure' Type IaA spectra are assumed to contain unresolved B-centers that account for less than 1% of the total nitrogen. **(a)** Assuming 'Finsch IaA' and 'Finsch IaAB' diamonds formed at the same time, the two groups of diamonds must have experienced a difference of 110–130°C in their mantle residence temperatures for a minimum mantle residence time of ~20 Myr. Their mantle residence times increase significantly with decreasing temperatures. **(b)** Assuming similar residence temperature for both diamond groups, the minimum time gap between the formation of 'Finsch IaA' and 'Finsch IaAB' diamonds is ~15 Myr at 1250°C and up to ~1.5 Gyr at 1130°C; lower temperatures are unlikely as they require the formation of the 'Finsch IaAB' diamonds before 3 Gyr

aggregation and HDF compositional variations within the microinclusion-bearing diamonds in Finsch, and allows their formation at similar lithospheric depth. The finding of saline and low-Mg carbonatite HDFs in two separate growth layers, with different nitrogen aggregations, within a single octahedral diamond from Finsch (Weiss et al. 2014) supports this scenario. Thus, we suggest that 'Finsch IaA' diamonds formed during a young saline metasomatic event which preceded kimberlite eruption by ~50 kyr to 15 Myr. The timing of metasomatism and formation of the 'Finsch IaAB' diamonds by carbonatite HDFs is less constrained, and could have taken place between ~15 Myr and 2 Gyr before the Finsch kimberlite erupted.

Saline HDFs of comparable compositions to those in 'Finsch IaA' diamonds are found in microinclusions in an octahedral diamond from Finsch (Fig. 3; Weiss et al. 2014), and in microinclusions-bearing diamonds from De Beers Pool and Koffiefontein, associated with both peridotite and eclogite host-rocks (Izraeli et al. 2001, 2004; Weiss et al. 2018). We note that saline compositions in De Beers Pool diamonds are higher in CaO and Na_2O, and lower in K_2O and FeO, compared to saline HDFs in Finsch diamonds (Fig. 4). However, all of these diamonds show nitrogen aggregation solely in A-centers (type IaA), indicating relatively short mantle residence times and formation during recent metasomatism by saline fluids. Halide-rich fluid inclusions in MARID nodules (Konzett et al. 2014) and the presence of mineral phases enriched in alkalis, Cl and volatile species in mantle xenoliths from De Beers Pool (e.g. Giuliani et al. 2013) are another manifestation of this saline metasomatism in the southwest Kaapvaal deep lithosphere. Earlier metasomatic events in this

lithosphere province, by carbonatitic and silicic melts/fluids, are evident by the presence of carbonatitic and silicic HDF microinclusions in fibrous diamonds (Fig. 3 - 'Finsch IaAB' diamonds; Weiss et al. 2018), the presence of phlogopite and carbonate inclusions in fibrous and octahedral diamonds (Fig. 1; Weiss et al. 2018; Wang et al. 1996), and by the finding of metasomatic minerals and chemical fingerprints in garnets within xenoliths from Finsch and De Beers Pool kimberlites (e.g. Giuliani et al. 2014; Griffin et al. 1999; Jollands et al. 2018).

Mineral microinclusions associated with HDFs in fibrous diamonds show enrichment in incompatible elements, for example: clinopyroxene microinclusions, associated with saline HDFs in microinclusion-bearing diamonds from the Panda kimberlite (Slave Craton, Canada), are strongly enriched in LREEs with a steep REE trend ($La/Lu_{(CN)} \approx 90$; Tomlinson et al. 2009). Such incompatible element enrichment in mantle minerals reflects HDF–rock interaction and the impact of this process in shaping trace element enriched mantle metasomatic reservoirs. On the other hand, it is commonly accepted that the major element compositions of such minerals reflects their mantle host rock lithology and its origin. For example, the variation of MgO and Na_2O content in omphacite (Fig. 7c), between diopside and jadeite end-member components, is controlled by its host eclogite type, varying between garnet-pyroxenite of mantle origin (Group A) and kyanite and corundum eclogites of subducted crust origin (Group C; Aulbach et al. 2016; Coleman et al. 1965; Grütter and Quadling 1999; Jacob 2004; Macgregor and Carter 1970; Taylor and Neal 1989). Two of the diamonds studied here encapsulated omphacite microinclusions in association with saline HDF (ON-FCH-351) or with low-Mg carbonatitic-like HDF (ON-FCH-350; Fig. 1). They have Si per 12 oxygen formula units of 3.97 ± 0.07 (1σ) and Mg#-values in the same range as many clinopyroxenes in mantle eclogite xenoliths (Fig. 7b). However most omphacites associated with saline or low-Mg carbonatitic-like HDFs have low Mg# (80 ± 5 on average), below the median value of clinopyroxene in mantle eclogites (Mg# = 85; Aulbach and Jacob 2016 and unpublished data). These omphacites have MgO and Na_2O values that are classified into Group B eclogite (intermediate between Group A and Group C); with the ones associated with saline HDFs having higher Na_2O at similar MgO values (Fig. 7c). Separation between the two omphacite groups is further observed in CaO vs. MgO, Al_2O_3 vs. MgO and Al_2O_3 vs. CaO spaces, within the compositional variation array of clinopyroxene in mantle eclogites (Fig. 7d-f), thus suggesting a possible relationship between omphacite composition and the type of metasomatic agent it interacted with. For evaluating such a relationship, we selected 20 data points from the clinopyroxene-in-mantle-eclogite-xenoliths dataset of Aulbach and Jacob (2016 and unpublished data), that have CaO and MgO values similar to omphacite associated with saline HDFs (10 data points) or low-Mg carbonatitic-like HDFs (10 data points; Fig. 7d). The data points mostly overlap or fall close to the two omphacite groups on Al_2O_3 vs. MgO and Al_2O_3 vs. CaO variations (Fig. 7e,f), reinforcing the possible connection between omphacite composition and its metasomatising fluid/melt type. In addition, we note that omphacites in high-Mg mantle eclogites, which were identified as metasomatised by kimberlite or high-Mg carbonatite (Aulbach and Jacob 2016 and unpublished data), mostly have high-CaO and low-Al_2O_3 values that are separated from omphacites associated with either saline or low-Mg carbonatitic-like HDFs (Fig. 7f). Additional data is necessary for clarifying the role of different metasomatic agent types in shaping the major element composition of eclogitic clinopyroxene. Nonetheless, based on the above observation we suggest that Al_2O_3 vs. CaO variations of metasomatic omphacite likely reflect the composition of the metasomatising fluid/melt, and can be used to infer its nature. This alternative, in addition to trace element patterns of mantle minerals, is appealing for interpreting the type of fluid/melt responsible for metasomatism, as remnants of metasomatic mantle agents are only rarely observed in mantle samples (e.g. van Achterbergh et al. 2002), and trace element patterns and fingerprints of different metasomatic agent types can be similar (e.g. carbonatite, silicic and saline; e.g. Weiss et al. 2013).

Combining the data for microinclusion-bearing diamonds from the Finsch Group II kimberlite (this study) and the neighboring Group I kimberlites in Koffiefontein and De Beers Pool (Izraeli et al. 2001, 2004; Weiss et al. 2018), suggests that a substantial volume of the southwest Kaapvaal deep lithosphere was impacted by saline metasomatism during Cretaceous time. Moreover, it indicates direct relationships between metasomatism by highly saline fluids, diamond formation and the late-Mesozoic 'bloom' of kimberlite eruptions on the Kaapvaal Craton (Griffin et al. 2014). A similar relationship is possible between saline metasomatism in the central Slave Craton, as evident from the majority of saline microinclusions-bearing type-IaA diamonds from the Ekati and Diavik mines (Weiss et al. 2015), and Cenozoic kimberlite eruptions in this lithospheric province. A strong connection, however, has been established between metasomatised carbonated peridotite sources, high-Mg carbonatitic HDFs and the formation of kimberlitic melts (e.g. Brey et al. 2008; Dalton and Presnall 1998; Dvir and Kessel 2017; Greenwood et al. 1999; Kamenetsky et al. 2004; Pokhilenko et al. 2015; Weiss et al. 2011). Indeed, saline HDFs invaded a carbonated and metasomatised lithosphere in the Kaapvaal Craton prior to the kimberlite eruptions, as discussed above. This also occurred in the central Slave Craton (Weiss et al. 2015). We therefore suggest that saline HDFs, in addition to carbonatitic metasomatism, play a key role in the metasomatic 'cocktail' of mantle sources leading to kimberlite eruptions.

Acknowledgements We thank William L. Griffin and Suzanne Y. O'Reilly for the use of the LA-ICP-MS at Macquarie University, Daniel Howell for the use of a modified version of DiaMap, and Jeffrey W. Harris for the donation of diamonds used in this study. This study was supported by National Science Foundation grants EAR13-48045 and EAR17-25323 to Y.W. and S.L.G. FTIR analyses were supported through the German Israeli Foundation grant GIF I-1239-301.8/2014 to O.N. The handling guest editor Thomas Stachel and two anonymous reviewers made excellent suggestions that greatly improved this paper. This is Lamont–Doherty Earth Observatory contribution number (# 8230).

References

Akagi T, Masuda A (1988) Isotopic and elemental evidence for a relationship between kimberlite and Zaire cubic diamonds. Nature 336(6200):665–667

Appleyard CM, Viljoen KS, Dobbe R (2004) A study of eclogitic diamonds and their inclusions from the Finsch kimberlite pipe, South Africa. Lithos 77(1):317–332

Aulbach S, Jacob DE (2016) Major- and trace-elements in cratonic mantle eclogites and pyroxenites reveal heterogeneous sources and metamorphic processing of low-pressure protoliths. Lithos 262(Supplement C):586–605

Aulbach S, Shirey SB, Stachel T, Creighton S, Muehlenbachs K, Harris JW (2009) Diamond formation episodes at the southern margin of the Kaapvaal craton: Re–Os systematics of sulfide inclusions from the Jagersfontein Mine. Contrib Mineral Petr 157(4):525–540

Aulbach S, Gerdes A, Viljoen K (2016) Formation of diamondiferous kyanite–eclogite in a subduction mélange. Geochim Cosmochim Ac 179:156–176

Bastin G, Heijligers J (1991) Quantitative electron probe microanalysis of ultralight elements (boron-oxygen). In: Heinrich K, Newbury D (eds) Electron probe quantitation, Workshop at the National Bureau of Standards, Gaithersburg. Maryland. Plenum Press, New York, pp 145–161

Boyd SR, Kiflawi I, Woods GS (1994) The relationship between infrared-absorption and the A defect concentration in diamond. Philos Mag B 69(6):1149–1153

Boyd SR, Kiflawi I, Woods GS (1995) Infrared absorption by the B nitrogen aggregate in diamond. Philos Mag B 72(3):351–361

Brey GP, Bulatov VK, Girnis AV, Lahaye Y (2008) Experimental melting of carbonated peridotite at 610 GPa. J Petrol 49(4):797–821

Carlson RW, Pearson DG, James DE (2005) Physical, chemical, and chronological characteristics of continental mantle. Rev Geophys 43(1):1–24

Coleman RG, Lee DE, Beatty LB, Brannock WW (1965) Eclogites and eclogites: their differences and similarities. Geol Soc Am Bull 76(5): 483–508

Dalton JA, Presnall DC (1998) The continuum of primary carbonatitic-kimberlitic melt compositions in equilibrium with lherzolite: data from the system CaO-MgO-Al_2O_3-SiO_2-CO_2 at 6 GPa. J Petrol 39(11–12):1953–1964

Dawson JB (1984) Contrasting types of upper-mantle metasomatism? In: Kornprobst J (ed) developments in petrology. vol 11. Elsevier, pp 289–294

Deines P (1980) The carbon isotopic composition of diamonds: relationship to diamond shape, color, occurrence and vapor composition. Geochim Cosmochim Ac 44(7):943–961

Deines P, Gurney JJ, Harris JW (1984) Associated chemical and carbon isotopic composition variations in diamonds from Finsch and Premier kimberlite, South Africa. Geochim Cosmochim Ac 48(2): 325–342

Dvir O, Kessel R (2017) The effect of CO_2 on the water-saturated solidus of K-poor peridotite between 4 and 6 GPa. Geochim Cosmochim Ac 206:184–200

Evans T (1992) Aggregation of nitrogen in diamond. In: Field JE (ed) The properties of natural and synthetic diamond. Academic Press, London, pp 259–290

Giuliani A, Kamenetsky VS, Kendrick MA, Phillips D, Goemann K (2013) Nickel-rich metasomatism of the lithospheric mantle by pre-kimberlitic alkali-S–Cl-rich C–O–H fluids. Contrib Mineral Petr 165(1):155–171

Giuliani A, Phillips D, Maas R, Woodhead JD, Kendrick MA, Greig A, Armstrong RA, Chew D, Kamenetsky VS, Fiorentini ML (2014) LIMA U–Pb ages link lithospheric mantle metasomatism to Karoo magmatism beneath the Kimberley region, South Africa. Earth Planet Sc Lett 401:132–147

Green DH, Wallace ME (1988) Mantle metasomatism by ephemeral carbonatite melts. Nature 336:459–462

Greenwood JC, Gibson SA, Thompson RN, Weska RK, Dickin AP (1999) Cretaceous kimberlites from the Paranatinga–Batovi region, Central Brazil: geochemical evidence for subcratonic lithospheric mantle heterogeneity. In: Dawson JB (ed) Proceedings of the VIIth international kimberlite conference, vol 1, pp 291–298

Grégoire M, Bell D, Le Roex A (2002) Trace element geochemistry of phlogopite-rich mafic mantle xenoliths: their classification and their relationship to phlogopite-bearing peridotites and kimberlites revisited. Contrib Mineral Petr 142(5):603–625

Griffin WL, Gurney JJ, Ryan CG (1992) Variations in trapping temperatures and trace elements in peridotite-suite inclusions from African diamonds: evidence for two inclusion suites, and implications for lithosphere stratigraphy. Contrib Mineral Petr 110(1):1–15

Griffin WL, Shee RS, Ryan GC, Win TT, Wyatt AB (1999) Harzburgite to lherzolite and back again: metasomatic processes in ultramafic xenoliths from the Wesselton kimberlite, Kimberley, South Africa. Contrib Mineral Petr 134(2):232–250

Griffin WL, Powell WJ, Pearson NJ, O'Reilly SY (2008) GLITTER: data reduction software for laser ablation ICP-MS. Appendix 2 in: Sylvester P (ed) laser ablation-ICP-MS in the earth sciences: mineralogical association of Canada short course series, vol 40, pp 204-207

Griffin WL, Batumike JM, Greau Y, Pearson NJ, Shee SR, O'Reilly SY (2014) Emplacement ages and sources of kimberlites and related rocks in southern Africa: U–Pb ages and Sr–Nd isotopes of groundmass perovskite. Contrib Mineral Petr 168(1):1032

Grütter H, Quadling K (1999) Can sodium in garnet be used to monitor eclogitic diamond potential. In: Dawson JB (ed) proceedings of the VIIth international kimberlite conference, vol 1, pp 314–320

Gurney JJ, Harris JW, Rickard RS (1979) Silicate and oxide inclusions in diamonds from the Finsch kimberlite pipe. In: Boyd FR, HOA M (eds) Kimberlites, diatremes, and diamonds: their geology, petrology, and geochemistry. American Geophysical Union, pp 1–15

Gurney JJ, Helmstaedt HH, Richardson SH, Shirey SB (2010) Diamonds through time. Econ Geol 105(3):689–712

Howell D, O'Neill CJ, Grant KJ, Griffin WL, Pearson NJ, O'Reilly SY (2012) μ-FTIR mapping: distribution of impurities in different types of diamond growth. Diam Relat Mater 29(Supplement C):29–36

Izraeli ES, Harris JW, Navon O (2001) Brine inclusions in diamonds: a new upper mantle fluid. Earth Planet Sc Lett 187(3):323–332

Izraeli ES, Harris JW, Navon O (2004) Fluid and mineral inclusions in cloudy diamonds from Koffiefontein, South Africa. Geochim Cosmochim Ac 68(11):2561–2575

Jablon BM, Navon O (2016) Most diamonds were created equal. Earth Planet Sc Lett 443:41–47

Jacob D (2004) Nature and origin of eclogite xenoliths from kimberlites. Lithos 77(1–4):295–316

Jollands MC, Hanger BJ, Yaxley GM, Hermann J, Kilburn MR (2018) Timescales between mantle metasomatism and kimberlite ascent

indicated by diffusion profiles in garnet crystals from peridotite xenoliths. Earth Planet Sc Lett 481(Supplement C):143–153

Kamenetsky MB, Sobolev AV, Kamenetsky VS, Maas R, Danyushevsky LV, Thomas R, Pokhilenko NP, Sobolev NV (2004) Kimberlite melts rich in alkali chlorides and carbonates: a potent metasomatic agent in the mantle. Geology 32(10):845–848

Kiflawi I, Mayer AE, Spear PM, Van Wyk JA, Woods GS (1994) Infrared absorption by the single nitrogen and A defect centres in diamond. Philos Mag B 69(6):1141–1147

Klein-BenDavid O, Izraeli ES, Hauri E, Navon O (2007) Fluid inclusions in diamonds from the Diavik mine, Canada and the evolution of diamond-forming fluids. Geochim Cosmochim Ac 71(3):723–744

Klein-BenDavid O, Logvinova AM, Schrauder M, Spetius ZV, Weiss Y, Hauri EH, Kaminsky FV, Sobolev NV, Navon O (2009) High-Mg carbonatitic microinclusions in some Yakutian diamonds—a new type of diamond-forming fluid. Lithos 112:648–659

Konzett J, Krenn K, Rubatto D, Hauzenberger C, Stalder R (2014) The formation of saline mantle fluids by open-system crystallization of hydrous silicate-rich vein assemblages – evidence from fluid inclusions and their host phases in MARID xenoliths from the central Kaapvaal craton, South Africa. Geochim Cosmochim Ac 147:1–25

Kramers JD (1979) Lead, uranium, strontium, potassium and rubidium in inclusion-bearing diamonds and mantle-derived xenoliths from southern Africa. Earth Planet Sc Lett 42(1):58–70

Lazarov M, Woodland AB, Brey GP (2009) Thermal state and redox conditions of the Kaapvaal mantle: a study of xenoliths from the Finsch mine, South Africa. Lithos 112:913–923

Le Roex AP, Bell DR, Davis P (2003) Petrogenesis of group I kimberlites from Kimberley, South Africa: evidence from bulk-rock geochemistry. J Petrol 44(12):2261–2286

Luth RW (1993) Diamonds, eclogites, and the oxidation state of the Earth's mantle. Science 261(5117):66–68

Macgregor ID, Carter JL (1970) The chemistry of clinopyroxenes and garnets of eclogite and peridotite xenoliths from the Roberts Victor mine, South Africa. Phys Earth Planet IN 3:391–397

McDonough WF, Sun SS (1995) The composition of the Earth. Chem Geol 120(3–4):223–253

Menzies MA, Wass SY (1983) CO_2- and LREE-rich mantle below eastern Australia: a REE and isotopic study of alkaline magmas and apatite-rich mantle xenoliths from the southern Highlands Province, Australia. Earth Planet Sc Lett 65(2):287–302

Navon O, Hutcheon ID, Rossman GR, Wasserburg GJ (1988) Mantle-derived fluids in diamond micro-inclusions. Nature 335:784

Palot M, Pearson DG, Stern RA, Stachel T, Harris JW (2013) Multiple growth events, processes and fluid sources involved in diamond genesis: a micro-analytical study of sulphide-bearing diamonds from Finsch mine, RSA. Geochim Cosmochim Ac 106:51–70

Pearson DG, Shirey SB, Carlson RW, Boyd FR, Pokhilenko NP, Shimizu N (1995) Re-Os, Sm-Nd, and Rb-Sr isotope evidence for thick Archean lithospheric mantle beneath the Siberian craton modified by multistage metasomatism. Geochim Cosmochim Ac 59(5):959–977

Pearson DG, Shirey SB, Harris JW, Carlson RW (1998) Sulphide inclusions in diamonds from the Koffiefontein kimberlite, S Africa: constraints on diamond ages and mantle Re–Os systematics. Earth Planet Sc Lett 160(3–4):311–326

Phillips D, Harris J (1995) Geothermobarometry of diamond inclusions from the De Beers Pool mines, Kimberley, South Africa. In: Sixth international kimberlite conference, Novosibirsk, extended abstracts, pp 441–443

Phillips D, Harris JW, Viljoen KS (2004) Mineral chemistry and thermobarometry of inclusions from De Beers Pool diamonds, Kimberley, South Africa. Lithos 77(1–4):155–179

Pokhilenko NP, Agashev AM, Litasov KD, Pokhilenko LN (2015) Carbonatite metasomatism of peridotite lithospheric mantle: implications for diamond formation and carbonatite-kimberlite magmatism. Russ Geol Geophys 56(1):280–295

Rege S, Jackson S, Griffin WL, Davies RM, Pearson NJ, O'Reilly SY (2005) Quantitative trace-element analysis of diamond by laser ablation inductively coupled plasma mass spectrometry. J Anal Atom Spectrom 20(7):601–611

Rege S, Griffin WL, Pearson NJ, Araujo D, Zedgenizov D, O'Reilly SY (2010) Trace-element patterns of fibrous and monocrystalline diamonds: insights into mantle fluids. Lithos 118(3):313–337

Richardson SH, Gurney JJ, Erlank AJ, Harris JW (1984) Origin of diamonds in old enriched mantle. Nature 310(5974):198–202

Rickard RS, Harris JW, Gurney JJ, Cardoso P (1989) Mineral inclusions in diamonds from Koffiefontein mine. In: Ross J, Jacques AL, Ferguson J, Green DH, O'Reilly SY, Danchin RV, AJA J (eds) Kimberlites and related rocks, vol 2, Proceedings of the fourth international kimberlite conference. Geological society of Australia special publication 14. Perth, pp 1054–1062

Schneider ME, Eggler DH (1986) Fluids in equilibrium with peridotite minerals: implications for mantle metasomatism. Geochim Cosmochim Ac 50(5):711–724

Schrauder M, Koeberl C, Navon O (1996) Trace element analyses of fluid-bearing diamonds from Jwaneng, Botswana. Geochim Cosmochim Ac 60(23):4711–4724

Shee SR, Gurney JJ, Robinson DN (1982) Two diamond-bearing peridotite xenoliths from the Finsch kimberlite, South Africa. Contrib Mineral Petr 81(2):79–87

Shirey SB, Richardson SH, Harris JW (2004) Integrated models of diamond formation and craton evolution. Lithos 77(1–4):923–944

Simon NSC, Carlson RW, Pearson DG, Davies GR (2007) The origin and evolution of the Kaapvaal cratonic lithospheric mantle. J Petrol 48(3):589–625

Skuzovatov S, Zedgenizov D, Howell D, Griffin WL (2016) Various growth environments of cloudy diamonds from the Malobotuobia kimberlite field (Siberian craton). Lithos 265:96–107

Smit KV, Stachel T, Creaser RA, Ickert RB, DuFrane SA, Stern RA, Seller M (2014) Origin of eclogite and pyroxenite xenoliths from the Victor kimberlite, Canada, and implications for Superior craton formation. Geochim Cosmochim Ac 125:308–337

Smith CB, Allsopp HL, Kramers JD, Hutchinson G, Roddick JC (1985) Emplacement ages of Jurassic-Cretaceous South African kimberlites by the Rb-Sr method on phlogopite and whole-rock samples. S Afr J Geol 88:249–266

Smith CB, Gurney JJ, Harris JW, Otter ML, Kirkley MB, Jagoutz E (1991) Neodymium and strontium isotope systematics of eclogite and websterite paragenesis inclusions from single diamonds, Finsch and Kimberley Pool, RSA. Geochim Cosmochim Ac 55(9):2579–2590

Smith EM, Kopylova MG, Nowell GM, Pearson DG, Ryder J (2012) Archean mantle fluids preserved in fibrous diamonds from Wawa, Superior craton. Geology 40(12):1071–1074

Stachel T, Aulbach S, Brey GP, Harris JW, Leost I, Tappert R, Viljoen KS (2004) The trace element composition of silicate inclusions in diamonds: a review. Lithos 77(1):1–19

Taylor LA, Neal CR (1989) Eclogites with oceanic crustal and mantle signatures from the Bellsbank kimberlite, South Africa, part I: mineralogy, petrography, and whole rock chemistry. J Geol 97(5):551–567

Taylor WR, Jaques AL, Ridd M (1990) Nitrogen-defect aggregation characteristics of some Australian diamonds – time-temperature constraints on the source regions of pipe and alluvial diamonds. Am Mineral 75(11–12):1290–1310

Taylor WR, Canil D, Judith Milledge H (1996) Kinetics of Ib to IaA nitrogen aggregation in diamond. Geochim Cosmochim Ac 60(23):4725–4733

Thompson WK (1965) Infra-red spectroscopic studies of aqueous systems. Part 1- molar extinction coefficients of water, deuterium oxide,

deuterium hydrogen oxide, aqueous sodium chloride and carbon disulphide. T Faraday Soc 61(0):2635–2640

Tomlinson EL, Jones AP, Harris JW (2006) Co-existing fluid and silicate inclusions in mantle diamond. Earth Planet Sc Lett 250(3–4):581–595

Tomlinson EL, Müller W, EIMF (2009) A snapshot of mantle metasomatism: trace element analysis of coexisting fluid (LA-ICP-MS) and silicate (SIMS) inclusions in fibrous diamonds. Earth Planet Sc Lett 279(3–4):362–372

van Achterbergh E, Griffin WL, Ryan CG, O'Reilly SY, Pearson NJ, Kivi K, Doyle BJ (2002) Subduction signature for quenched carbonatites from the deep lithosphere. Geology 30(8):743–746

van Achterbergh E, Griffin WL, Ryan CG, O'Reilly SY, Pearson NJ, Kivi K, Doyle BJ (2004) Melt inclusions from the deep Slave lithosphere: implications for the origin and evolution of mantle-derived carbonatite and kimberlite. Lithos 76(1):461–474

Venyaminov SY, Prendergast FG (1997) Water (H_2O and D_2O) molar absorptivity in the 1000-4000 cm^{-1} range and quantitative infrared spectroscopy of aqueous solutions. Anal Biochem 248(2):234–245

Viljoen KS, Swash PM, Otter ML, Schulze DJ, Lawless PJ (1992) Diamondiferous garnet harzburgites from the Finsch kimberlite, Northern Cape, South Africa. Contrib Mineral Petr 110(1):133–138

Viljoen KS, Harris JW, Ivanic T, Richardson SH, Gray K (2014) Trace element chemistry of peridotitic garnets in diamonds from the Premier (Cullinan) and Finsch kimberlites, South Africa: contrasting styles of mantle metasomatism. Lithos 208:1–15

Wang A, Pasteris JD, Meyer HOA, Dele-Duboi ML (1996) Magnesite-bearing inclusion assemblage in natural diamond. Earth Planet Sc Lett 141(1):293–306

Wass SYH, Henderson P, Elliott CJ (1980) Chemical heterogeneity and metasomatism in the upper mantle: evidence from rare earth and other elements in apatite-rich xenoliths in basaltic rocks from eastern Australia. Philos T R Soc S-A 297(1431):333–346

Weiss Y, Kessel R, Griffin WL, Kiflawi I, Klein-BenDavid O, Bell DR, Harris JW, Navon O (2009) A new model for the evolution of diamond-forming fluids: evidence from microinclusion-bearing diamonds from Kankan, Guinea. Lithos 112:660–674

Weiss Y, Kiflawi I, Navon O (2010) IR spectroscopy: quantitative determination of the mineralogy and bulk composition of fluid microinclusions in diamonds. Chem Geol 275(1):26–34

Weiss Y, Griffin WL, Bell DR, Navon O (2011) High-Mg carbonatitic melts in diamonds, kimberlites and the sub-continental lithosphere. Earth Planet Sc Lett 309(3–4):337–347

Weiss Y, Griffin WL, Navon O (2013) Diamond-forming fluids in fibrous diamonds: the trace-element perspective. Earth Planet Sc Lett 376(Supplement C):110–125

Weiss Y, Kiflawi I, Davies N, Navon O (2014) High-density fluids and the growth of monocrystalline diamonds. Geochim Cosmochim Ac 141(Supplement C):145–159

Weiss Y, McNeill J, Pearson DG, Nowell GM, Ottley CJ (2015) Highly saline fluids from a subducting slab as the source for fluid-rich diamonds. Nature 524(7565):339–342

Weiss Y, Navon O, Goldstein SL, Harris JW (2018) Inclusions in diamonds constrain thermo-chemical conditions during Mesozoic metasomatism of the Kaapvaal cratonic mantle. Earth Planet Sc Lett 491:134–147

Wyllie PJ (1977) Mantle fluid compositions buffered by carbonates in peridotite-CO_2–H_2O. The J Geol 85(2):187–207

Zedgenizov DA, Ragozin AL, Shatsky VS, Araujo D, Griffin WL, Kagi H (2009) Mg and Fe-rich carbonate–silicate high-density fluids in cuboid diamonds from the Internationalnaya kimberlite pipe (Yakutia). Lithos 112:638–647